The UV continuum slopes of early star-forming galaxies in JADES

Michael W. Topping [,1]★ Daniel P. Stark,[1] Ryan Endsley [,2] Lily Whitler [,1] Kevin Hainline,[1] Benjamin D. Johnson,[3] Brant Robertson,[4] Sandro Tacchella [,5,6] Zuyi Chen [,1] Stacey Alberts [,1] William M. Baker [,5,6] Andrew J. Bunker,[7] Stefano Carniani [,8] Stephane Charlot [,9] Jacopo Chevallard [,7] Emma Curtis-Lake [,10] Christa DeCoursey,[1] Eiichi Egami,[1] Daniel J. Eisenstein [,3] Zhiyuan Ji,[1] Roberto Maiolino,[5,6,11] Christina C. Williams,[12] Christopher N. A. Willmer,[1] Chris Willott[13] and Joris Witstok [5,6]

[1]*Steward Observatory, University of Arizona, 933 N Cherry Avenue, Tucson, AZ 85721, USA*
[2]*Department of Astronomy, University of Texas, Austin, TX 78712, USA*
[3]*Center for Astrophysics | Harvard & Smithsonian, 60 Garden St, Cambridge, MA 02138, USA*
[4]*Department of Astronomy and Astrophysics, University of California, Santa Cruz, 1156 High Street, Santa Cruz, CA 95064, USA*
[5]*Kavli Institute for Cosmology, University of Cambridge, Madingley Road, Cambridge CB3 0HA, UK*
[6]*Cavendish Laboratory, University of Cambridge, 19 JJ Thomson Avenue, Cambridge CB3 0HE, UK*
[7]*Department of Physics, University of Oxford, Denys Wilkinson Building, Keble Road, Oxford OX1 3RH, UK*
[8]*Scuola Normale Superiore, Piazza dei Cavalieri 7, I-56126 Pisa, Italy*
[9]*Institut d'Astrophysique de Paris, CNRS, UMR 7095, Sorbonne Université, 98 bis bd Arago, F-75014 Paris, France*
[10]*Centre for Astrophysics Research, Department of Physics, Astronomy and Mathematics, University of Hertfordshire, Hatfield AL10 9AB, UK*
[11]*Department of Physics and Astronomy, University College London, Gower Street, London WC1E 6BT, UK*
[12]*NSF's National Optical-Infrared Astronomy Research Laboratory, 950 North Cherry Avenue, Tucson, AZ 85719, USA*
[13]*NRC Herzberg, 5071 West Saanich Rd, Victoria, BC V9E 2E7, Canada*

ABSTRACT

The power-law slope of the rest-ultraviolet (UV) continuum ($f_\lambda \propto \lambda^\beta$) is a key metric of early star-forming galaxies, providing one of our only windows into the stellar populations and physical conditions of $z \gtrsim 10$ galaxies. Expanding upon previous studies with limited sample sizes, we leverage deep imaging from the *JWST* Advanced Deep Extragalactic Survey (JADES) to investigate the UV slopes of 179 $z \gtrsim 9$ galaxies with apparent magnitudes of $m_{F200W} \simeq 26$–31, which display a median UV slope of $\beta = -2.4$. We compare to a statistical sample of $z \simeq 5$–9 galaxies, finding a shift towards bluer rest-UV colours at all M_{UV}. The most UV-luminous $z \gtrsim 9$ galaxies are significantly bluer than their lower redshift counterparts, representing a dearth of moderately red galaxies within the first 500 Myr. At yet earlier times, the $z \gtrsim 11$ galaxy population exhibits very blue UV slopes, implying very low impact from dust attenuation. We identify a robust sample of 44 galaxies with $\beta \lesssim -2.8$, which have spectral energy distributions requiring models of density-bounded H II regions and median ionizing photon escape fractions of 0.51 to reproduce. Their rest-optical colours imply that this sample has weaker emission lines (median $m_{F356W} - m_{F444W} = 0.19$ mag) than typical galaxies (median $m_{F356W} - m_{F444W} = 0.39$ mag), consistent with the inferred escape fractions. This sample consists of relatively low stellar masses (median $\log(M/M_\odot) = 7.5 \pm 0.2$), and specific star formation rates (sSFRs; median = 79 Gyr^{-1}) nearly twice that of our full galaxy sample (median sSFRs = 44 Gyr^{-1}), suggesting these objects are more common among systems experiencing a recent upturn in star formation. We demonstrate that the shutoff of star formation provides an alternative solution for modelling of extremely blue UV colours, making distinct predictions for the rest-optical emission of these galaxies. Future spectroscopy will be required to distinguish between these physical pictures.

Key words: galaxies: evolution – galaxies: high-redshift.

1 INTRODUCTION

The slope of the rest-ultraviolet (UV) continuum (parametrized as β where $f_\lambda \propto \lambda^\beta$) provides a valuable diagnostic of star-forming

galaxies. At the highest redshifts accessible with current telescopes (i.e. $z \gtrsim 11$), the UV continuum is often the only detectable part of the spectrum, with the slope providing a rare clue as to the nature of the earliest systems. The intrinsic UV spectral slope is set by the properties of the massive star populations (e.g. metallicity and age) with additional contributions from the spectral shape of nebular continuum emission at very young ages. The presence of dust then

★ E-mail: michaeltopping@arizona.edu

reddens the intrinsic spectrum to its observed form. For the majority of star-forming galaxies, dust plays the dominant role in driving variations in the observed UV colours (e.g. Wilkins et al. 2011), with stellar properties (Calabrò et al. 2021) and ionized gas conditions (e.g. Chisholm et al. 2022) having an important but second-order effect.

Deep imaging surveys with the *Hubble Space Telescope (HST)* have allowed UV continuum slopes to be computed for large samples of star-forming galaxies in the reionization era (e.g. McLure et al. 2011; Dunlop et al. 2012; Finkelstein et al. 2012; Rogers, McLure & Dunlop 2013; Bouwens et al. 2014; Bhatawdekar & Conselice 2021). These studies have indicated that $z \simeq 7$–8 galaxies are considerably bluer than those at $z \simeq 2$–3 (e.g. Dunlop et al. 2012; Bouwens et al. 2014), with reionization-era UV slopes often having $\beta \lesssim -2$. Dust is likely the primary factor driving this observed redshift evolution in UV slopes, with $z \simeq 7$–8 galaxies facing less attenuation than those at later epochs. Some investigations have found a trend towards bluer UV slopes at lower UV luminosities, with the faintest sources ($M_{UV} \simeq -18.0$) at $z \simeq 7$–8 exhibiting UV slopes ($\beta \simeq -2.4$) that approach the intrinsic values expected for stellar populations and nebular continuum emission (e.g. Cullen et al. 2017). These results potentially indicate a trend between dust attenuation and UV luminosity that has significant implications for the integrated star formation rate (SFR) density and may hint at a relationship between luminosity and metals in reionization-era systems. However, others have argued that the UV slope distribution in the reionization era is entirely consistent with a population average of $\beta \simeq -2$, with photometric scatter driving the range of UV slopes seen in the galaxy population (e.g. Cullen et al. 2023).

At yet earlier epochs ($z \gtrsim 9$) we may expect to see additional evolution in the distribution of UV slopes. If the massive stellar populations evolve significantly towards lower metallicities at higher redshift, we may find a shift blueward in colours. On the other hand, if the light-weighted stellar population ages become very young, we may expect nebular continuum emission to slightly redden UV slopes. And finally, if dust has yet to build up in even the most luminous galaxies at $z \gtrsim 9$, there may be no observed trend between UV luminosity and UV colour, with all galaxies showing mostly unattenuated spectral energy distributions (SEDs). Unfortunately *HST* has never been able to address these questions on its own. Not only are its photometric samples too small at $z \gtrsim 9$ (e.g. Bhatawdekar & Conselice 2021), but its cut-off at wavelengths redder than the *H* band precluded photometric measurements in the wavelength range (2–3 μm) needed for establishing UV colours at these redshifts. The combination of *HST* and *Spitzer* photometry provided a first window on UV slopes at $z \simeq 10$ (Wilkins et al. 2016; Tacchella et al. 2022), but such efforts were limited to very small samples given the sensitivity of *Spitzer* imaging.

The launch of the *JWST* (Gardner et al. 2023) has quickly revolutionized the study of galaxies at $z \gtrsim 9$. Thanks to the unprecedented sensitivity of the Near Infrared Camera (NIRCam; Rieke, Kelly & Horner 2005; Rieke et al. 2023b) at 2–5 μm, it is now possible to investigate the distribution of UV slopes in large samples of galaxies at $z \gtrsim 9$. The first *JWST* imaging campaigns led to a number of investigations into the UV slopes of $z \gtrsim 9$ galaxies (Bouwens et al. 2022; Topping et al. 2022; Cullen et al. 2023; Furtak et al. 2023; Nanayakkara et al. 2023). A key emerging result from these early programs is the striking commonality of blue UV slopes, with typical values of $\beta \leq -2.0$, now extended to the earliest times (e.g. Arrabal Haro et al. 2023; Curtis-Lake et al.

2023; Robertson et al. 2023b). The UV continua of these objects provide powerful insight into the physical conditions of galaxies at the highest redshifts, such as low impact from dust and young stellar population ages. This advancement has further allowed the identification and confirmation of extremely blue galaxies (e.g. Topping et al. 2022), whose existence was difficult to establish with *HST* alone.

The origin of galaxies with $\beta \lesssim -3$ has tested galaxy evolution models since their emergence among $z \gtrsim 7$ samples of faint objects (Bouwens et al. 2010; Labbé et al. 2010; Ono et al. 2010). These extreme systems have long proven challenging to explain with standard model treatment of emission from stars and gas (e.g. Robertson et al. 2010; Wilkins et al. 2011; Zackrisson, Inoue & Jensen 2013). While many physical explanations have been provided, one promising solution has been the result of significant leakage of Lyman continuum (LyC) radiation (e.g. Raiter, Schaerer & Fosbury 2010; Zackrisson et al. 2017; Plat et al. 2019). Several observational campaigns have explored this phenomenon in the local Universe, where direct confirmation of ionizing photon leakage is possible (e.g. Yamanaka et al. 2020; Chisholm et al. 2022; Flury et al. 2022b). Recently, Kim et al. (2023) measured UV slopes on small scales within a confirmed LyC leaker at $z = 2.37$ and demonstrated that indeed the UV continua of the leaking regions are extremely blue and consistent with little-to-no nebular continuum. Early *JWST* programs have enabled the identification and study of this class of objects into the distant Universe (e.g. Topping et al. 2022; Furtak et al. 2023); however, progress has been stifled due to low sample statistics and uncertainties due to photometric scatter.

In this work, we utilize imaging from the *JWST* Advanced Deep Extragalactic Survey (JADES; Eisenstein et al. 2023) to address several key shortcomings of current UV slope analyses. Imaging from JADES has already been demonstrated as an effective tool for identifying and discerning the properties of high-redshift galaxies (e.g. Endsley et al. 2023b; Hainline et al. 2023; Robertson et al. 2023b; Tacchella et al. 2023). We leverage the JADES data to explore the UV slopes for a statistical sample of galaxies at $z \sim 5$–14 and cover a large dynamic range of UV luminosity, enabling us to explore trends among the high-redshift galaxy population. Using this large parent sample, we identify a significant number of extremely blue ($\beta \simeq -3$) galaxies with robust UV slope measurements, which otherwise may suffer from cosmic variance among smaller samples (e.g. Topping et al. 2022). We place the observed SEDs of this blue sample in the context of models that allow for the escape of LyC photons, and those with complex star formation histories (SFHs). Finally, we discuss the galaxy properties implied by these two physical pictures, and the different observed quantities that may be able to distinguish them.

This paper is organized as follows. Section 2 describes the data and reduction techniques, as well as the sample selection and methods to derive galaxy properties. In Section 3, we present the UV slopes of our sample and discuss trends with UV luminosity and their redshift evolution. Section 4 presents the selection of a sample of objects with extremely blue UV slopes, followed by a discussion of their properties and exploration of alternative interpretations of the data. Finally, we conclude with a summary of our key conclusions in Section 5. Throughout this paper we use AB magnitudes (Oke & Gunn 1983), and assume a cosmology with $\Omega_m = 0.3$, $\Omega_\Lambda = 0.7$, and $H_0 = 70$ km s^{-1} Mpc^{-1}. We additionally adopt solar abundances from Asplund et al. (2009), i.e. $Z_\odot = 0.014$.

2 DATA AND SAMPLE

2.1 Imaging and photometry

We utilized imaging data obtained as part of the JADES collaborative NIRCam + NIRSpec GTO program. While an in-depth description of the full data set and survey design are presented in Eisenstein et al. (2023), we provide a brief description here. The primary imaging data set was obtained using *JWST*/NIRCam within the Great Observatories Origins Deep Survey (Giavalisco et al. 2004) South field (GOODS-S: RA = 53°.126, Dec. = −27°.802) and North field (GOODS-N: RA = 189°.229, Dec. = +62°.238) obtained during the first year of *JWST* science operations. The full observational footprint was observed in four short-wavelength (SW) filters (*F090W*, *F115W*, *F150W*, and *F200W*) and four long-wavelength (LW) bands (*F277W*, *F356W*, *F410M*, and *F444W*). Data were also obtained in the *F335M* medium-band filter across a portion of the field, comprising ∼81 per cent of the full observational footprint.

The JADES NIRCam imaging used in this work was obtained between 2022 October and 2023 February, and reductions of these data have been described in several recent publications (Endsley et al. 2023b; Rieke et al. 2023a; Robertson et al. 2023b; Tacchella et al. 2023; Williams et al. 2023). For this analysis, we employed final mosaics and photometric catalogues produced following the steps discussed in Endsley et al. (2023b), for which we provide a brief description here. Briefly, the raw uncalibrated exposure frames were first processed through the *JWST* calibration pipeline utilizing updated reference files based on in-flight performance. The resulting images were then corrected for unwanted artefacts, such as wisps and 'snowballs' (e.g. Bagley et al. 2023; Rigby et al. 2023). Following this, each image was flat-fielded using custom sky flats and flux calibrated, after which a correction for 1/*f* noise was implemented. The calibrated images were combined into final mosaics on a 0.03 arcsec pixel scale, and aligned to the *Gaia*-Early Data Release 3 (EDR3) reference frame. Finally, all of the mosaics were convolved to the point spread function of the *F444W* filter following the procedures outlined in Endsley et al. (2023a). The *JWST*/NIRCam data set was supplemented by public archival imaging available in the *HST* Legacy Fields (Illingworth et al. 2013; Whitaker et al. 2019). Specifically, we utilized mosaics in the GOODS-S field obtained in the *HST*/Advanced Camera for Surveys (ACS) *F435W*, *F606W*, *F775W*, *F814W*, and *F850LP* filters. As with the *JWST*/NIRCam imaging mosaics, the archival *HST* images were shifted into a consistent astrometric reference frame based on the *Gaia*-EDR3 astrometry, and placed on the same pixel scale as the *JWST*/NIRCam mosaics.

The source catalogue was derived by first constructing a detection image composed of an inverse variance weighted stack of the *F200W*, *F277W*, *F335M*, *F356W*, *F410M*, and *F444W* NIRCam mosaics. Sources were subsequently identified from this detection image using SEXTRACTOR (SOURCE EXTRACTOR; Bertin & Arnouts 1996). Photometric fluxes for each source were computed in Kron (1980) apertures in each filter, with uncertainties derived by placing copies of a large number of apertures among blank regions of the mosaic surrounding the object, and taking the standard deviation of the distribution of measured fluxes. These observations obtained as part of the main JADES program reach a typical point source depth (5σ) of ∼28.5 mag in the broad-band filters across the entire survey footprint, increasing to a depth of ∼30 mag in the deepest region of the mosaics. Further details regarding the extraction of photometry can be found in Endsley et al. (2023b).

2.2 Sample selection

The selection of high-redshift galaxies in JADES has yielded an abundant sample of galaxies at $z > 8$ identified based on their photometric redshifts (Hainline et al. 2023). In this work, we used a set of dropout selection criteria to identify galaxies from $z \sim 5$ to $z \sim 14$. Below, we compare the samples constructed from these two methodologies. Our selections consist of *F775W*, *F090W*, *F115W*, and *F150W* dropouts, which yield samples of galaxies roughly falling within redshift windows of $z \sim 5$–7, $z \sim 6.5$–8.5, $z \sim 8.5$–11, and $z \sim 11$–14. A detailed description of these selections is provided in Endsley et al. (2023b) and Whitler et al. (in preparation); however, we provide a brief description here.

Starting with the selection of the highest redshift galaxies, an initial selection of galaxies was obtained for the *F150W* dropout sample using the following criteria:

$$\begin{cases} \mathrm{S/N}_{F090W, F115W} < 2, \\ m_{F150W} - m_{F200W} > 1.3, \\ m_{F200W} - m_{F356W} < 1.0, \\ m_{F150W} - m_{F200W} > m_{F200W} - m_{F356W} + 1.3. \end{cases} \quad (1)$$

At slightly lower redshift, we selected galaxies within $z \sim 8$–11 as those that satisfy the *F115W* dropout criteria:

$$\begin{cases} \mathrm{S/N}_{F090W} < 2, \\ m_{F115W} - m_{F150W} > 1.3, \\ m_{F150W} - m_{F277W} < 1.0, \\ m_{F115W} - m_{F150W} > m_{F150W} - m_{F277W} + 1.3. \end{cases} \quad (2)$$

The lowest redshift selection that uses a *JWST*/NIRCam filter as a dropout band is the *F090W* dropouts, which were selected following:

$$\begin{cases} m_{F090W} - m_{F115W} > 1.3, \\ m_{F115W} - m_{F200W} < 1.0, \\ m_{F090W} - m_{F115W} > m_{F115W} - m_{F200W} + 1.3. \end{cases} \quad (3)$$

In addition, each of these selections required non-detections (S/N < 2) in ACS/*F435W*, *F606W*, and *F814W*, and optical χ^2 (Bouwens et al. 2015) of $\chi^2_{\mathrm{opt}} < 5$ calculated using the three ACS bands. Finally, a S/N > 3 detection is required in at least two *JWST*/LW bands, with a constraint of a S/N > 5 detection in *F200W*.

Finally, we selected a sample composed of *F775W* dropouts, intended to obtain galaxies at a redshift of $z \sim 5$–7. This sample was constructed using the following criteria:

$$\begin{cases} m_{F775W} - m_{F090W} > 1.2, \\ m_{F090W} - m_{F150W} < 1.0, \\ m_{F775W} - m_{F090W} > m_{F090W} - m_{F150W} + 1.2. \end{cases} \quad (4)$$

Following this initial selection, we employed several steps to clean each of these samples. First, we visually inspected the photometry and images of each source in the samples. From this visual inspection, we removed objects that were clear artefacts. This included objects identified as diffraction spikes, hot pixels, objects coincident with the detector edge, and residuals left over from the cosmic ray removal. We further removed objects from our sample that were significantly contaminated by flux from a bright neighbour, such that the flux from the candidate could not be separated out. We also fit BEAGLE (BayEsian Analysis of GaLaxy sEds; Chevallard & Charlot 2016) models to each of the candidate galaxies using the model set-up described in the following section. A further cut was applied based on the inferred photometric redshifts, such that we require a significant fraction of the total probability (>80 per cent) lying at a high redshift. This high-redshift cut-off was set at $z = 4$ for the *F775W* dropouts, and $z = 6$ for the *F090W*, *F115W*, and *F150W* dropouts. In total,
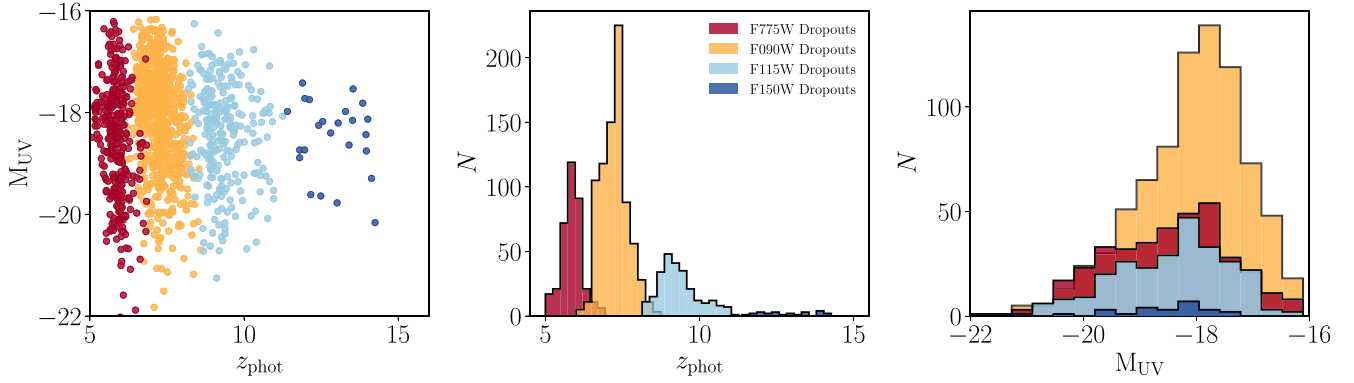
Figure 1. Galaxy demographics for the different samples used in this analysis, and described in Section 2.2. In each panel, we display the ACS/*F775W* dropout sample (red), NIRCam/*F090W* dropout sample (orange), NIRCam/*F115W* dropout sample (light blue), and NIRCam/*F150W* dropout sample (dark blue). The left panel illustrates the UV luminosity versus photometric redshift for the four samples derived from the SED fitting that is described in Section 2.3. Individual histograms of z_{phot} and M_{UV} comparing the four samples are presented in the centre and right panels, respectively.

this cleaning process resulted in a sample of 364, 656, 232, and 24 objects satisfying the *F775W*, *F090W*, *F115W*, and *F150W* dropout criteria and subsequent photometric redshift cut-off. We note that our dropout samples have a significant overlap with the sample of $z > 8$ galaxies presented in Hainline et al. (2023), which selected high-redshift galaxies from JADES based on their photometric redshifts as estimated from EAZY (Brammer, van Dokkum & Coppi 2008). We find that 92 per cent of our sample at $z > 8$ (corresponding to the selection criteria of Hainline et al. 2023) are in common with their selection. The remaining 8 per cent of the sample comprise objects at the edge of the dropout selection windows where the completeness is low, or very faint objects that are near the JADES detection limit.

2.3 Measured and inferred properties

Physical properties for our two high-redshift samples were obtained using a comprehensive suite of SED models. For all such properties inferred from SED modelling, we adopted values and uncertainties from the median and inner 68th percentile of the posterior probability distribution, respectively. We derive a fiducial set of model fits obtained using BEAGLE. These models employ stellar templates from the updated models of Bruzual & Charlot (2003) that have been post-processed to self-consistently include the effects of nebular emission following the procedures outlined in Gutkin, Charlot & Bruzual (2016). We employed a constant star formation history (CSFH) with a galaxy age that was allowed to vary from 1 Myr to the age of the Universe with a uniform prior in log space. For these models, we adopted a Chabrier (2003) initial mass function that covers a mass range of 0.1–300 $M_\odot$. We assumed that the stellar and gas-phase metallicities are the same, and adopt uniform priors in log space for metallicity and ionization parameter defined over the ranges of $\log(Z/Z_\odot) \in [-2.2, 0.3]$ and $\log(U) \in [-4, -1]$, respectively. These models implement the effects of dust using the Small Magellanic Cloud dust law (Pei 1992) as it has been demonstrated to accurately describe the observed properties of high-redshift galaxies (e.g. Bouwens et al. 2016; Reddy et al. 2018). Within the models, the effects of dust are parametrized by a τ_V, which is allowed to vary from 0.001 to 5 with a log-uniform prior. We allowed redshift to vary with a uniform prior within the range $z \in [0, 20]$. Finally, we assumed a fixed value for the dust-to-metal mass ratio of $\xi_d = 0.3$.

Table 1. Demographics of the four dropout samples, including median photometric redshifts, M_{UV}, and UV slope.

Selection	N	z_{phot}^{med}	M_{UV}^{med}	β_{med}
F775W dropouts	364	5.86	$-18.41^{+0.96}_{-1.29}$	$-2.26^{+0.03}_{-0.03}$
F090W dropouts	656	7.28	$-18.16^{+0.76}_{-1.04}$	$-2.32^{+0.03}_{-0.02}$
F115W dropouts	232	9.41	$-18.24^{+0.85}_{-1.35}$	$-2.35^{+0.04}_{-0.04}$
F150W dropouts	24	12.02	$-18.61^{+0.81}_{-0.91}$	$-2.48^{+0.12}_{-0.14}$

We display the demographics of our samples in Fig. 1. This figure presents the UV luminosities (M_{UV}) and photometric redshifts inferred from the best-fitting BEAGLE models. The average demographics for each of our dropout samples are presented in Table 1. We find median UV luminosities corresponding to $M_{UV} = -18.41$, -18.16, -18.24, and -18.61. The UV-luminous cut-off of the M_{UV} distributions trends toward fainter objects at earlier times consistent with measurements of the UV luminosity function at these epochs (e.g. Robertson et al. 2023a; Willott et al. 2023; Harikane et al. 2024). By virtue of their selection, we find median photometric redshifts of $z_{phot} = 5.86$, 7.28, 9.41, and 12.02 for the *F775W*, *F090W*, *F115W*, and *F150W* dropout samples, respectively. These same samples span redshift ranges of 5.05–6.84, 6.07–8.59, 8.20–11.25, and 11.40–14.25. It is clear that there is some overlap in the redshifts spanned by different dropout samples; however, we ensured that each individual galaxy was not identified in more than one sample.

We measured UV slopes for each object in the sample by fitting a power law ($f_\lambda \propto \lambda^\beta$; Calzetti, Kinney & Storchi-Bergmann 1994) to fluxes spanning the rest-UV portion of the SED. The set of filters that cover rest-UV fluxes depend on the redshift of the object and are chosen to avoid contamination from Lyα emission. For objects in our sample at $z < 5.4$, we measured the UV slope using the *F090W*, *F115W*, and *F150W* fluxes. For galaxies with photometric redshifts at $5.4 \leq z < 7.4$, we utilized the *F115W*, *F150W*, and *F200W* filters. At yet higher redshifts of $7.4 \leq z < 9.8$ and $9.8 \leq z < 13.2$, we measured UV slopes from the *F150W*, *F200W*, *F277W* and *F200W*, *F277W*, *F356W* filters, respectively. Finally, for the few galaxies in our sample at $z \geq 13.2$, *F277W*, *F356W*, and *F444W* were used. For each galaxy, we perturbed the photometry and remeasured the UV slope many times, and set the 1σ uncertainty according to the inner 68th percentile of the β measurements.
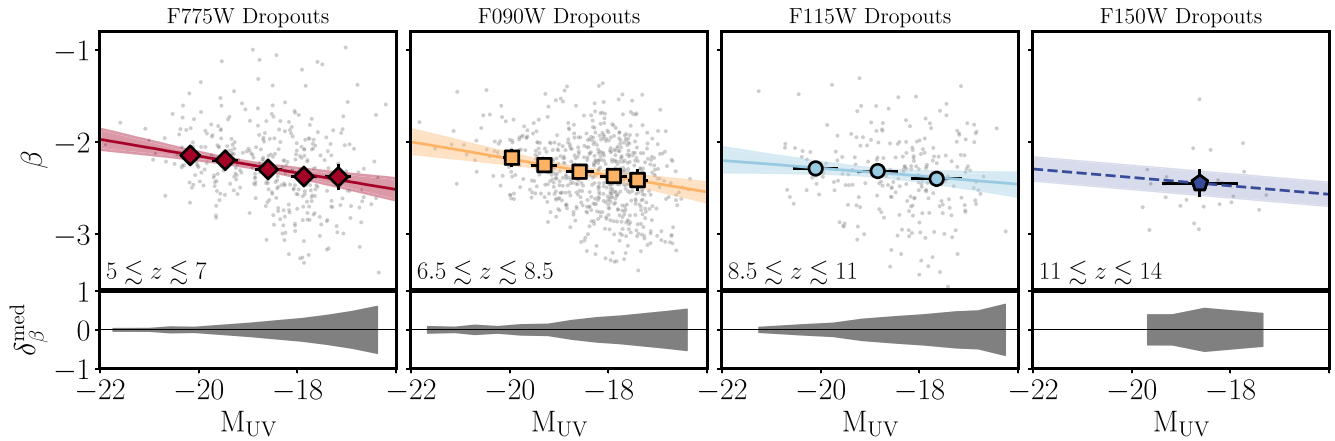
Figure 2. UV slopes of each object falling within our selections. Demographics of each dropout selection sample are provided in Table 1, and values for individual bins are given in Table 2. Linear fit parameters and uncertainties are presented in Table 3. The slope of the linear fit applied to the *F*150*W* dropout sample is fixed to that derived for the *F*115*W* dropouts. To distinguish this sample, we display its fit as a dashed line. The lower panel of each plot displays the median uncertainty in the UV slopes of individual objects as a function of UV luminosity.

3 UV SLOPES OF REIONIZATION-ERA GALAXIES

In this section, we leverage the imaging depth and area from the JADES program to explore the UV slopes of a statistical sample of $z > 9$ galaxies, allowing us to place meaningful constraints across a wide range of galaxy properties. We first discuss the UV slope distributions of each of the four dropouts samples individually, and explore trends between UV slope and UV luminosity at each redshift in Section 3.1. In Section 3.2, we combine the UV slope measurements of each of the dropout samples and constrain the redshift evolution over $5 \lesssim z \lesssim 14$.

3.1 UV slope distribution and M_{UV} trends

We present the UV slopes of our sample comprising 1276 galaxies identified at $z \sim 5$–14 across four dropout selections in Fig. 2. The median UV slopes for each dropout selection are provided in Table 1 and demonstrate that among each dropout sample, the typical UV slope is blue with a median β that ranges from -2.26 to -2.48. For the three lowest redshift samples, corresponding to *F*775*W*, *F*090*W*, and *F*115*W* dropouts, a sufficient number of galaxies are present for us to examine the UV luminosity dependence of their average UV slopes. The *F*150*W* dropout sample contains just 24 galaxies and only spans an M_{UV} range of -20.2 to -17.8 making it challenging to constrain a trend with M_{UV}. Table 2 gives properties of the bins within each dropout sample as well as the median β. We now discuss the UV slopes of each sample individually.

3.1.1 F775W dropouts

We present the UV slopes found for the *F*775*W* dropout sample in Fig. 2. These UV slopes have an inner 68th percentile range spanning in β from -1.7 to -2.7, and comprise a median UV slope of $\beta = -2.26^{+0.03}_{-0.03}$. This median value is broadly consistent with the UV slopes derived at $5.50 < z < 6.25$ from Nanayakkara et al. (2023) based on *JWST* data from the GLASS (Treu et al. 2023) program. Fig. 3 provides photometry and best-fitting SEDs for several galaxies in this sample across the range of observed UV slopes, illustrating the diversity of UV continua within. Qualitatively,

Table 2. Median UV slopes for each dropout sample divided into bins of UV luminosity. Uncertainties on M_{UV} and β are derived using the Monte Carlo bootstrap method described in Section 2.3.

Selection	N	z_{phot}^{med}	M_{UV}^{med}	β_{med}
*F*775*W* dropouts	46	6.01	$-20.24^{+0.23}_{-0.49}$	$-2.12^{+0.06}_{-0.06}$
	71	5.93	$-19.47^{+0.26}_{-0.24}$	$-2.20^{+0.05}_{-0.04}$
	89	5.82	$-18.59^{+0.26}_{-0.26}$	$-2.30^{+0.05}_{-0.05}$
	98	5.72	$-17.87^{+0.23}_{-0.24}$	$-2.38^{+0.07}_{-0.07}$
	43	5.85	$-17.19^{+0.26}_{-0.23}$	$-2.38^{+0.12}_{-0.13}$
*F*090*W* dropouts	53	7.57	$-19.95^{+0.14}_{-0.16}$	$-2.16^{+0.06}_{-0.08}$
	86	7.36	$-19.27^{+0.21}_{-0.26}$	$-2.25^{+0.04}_{-0.04}$
	160	7.32	$-18.57^{+0.26}_{-0.29}$	$-2.33^{+0.04}_{-0.04}$
	221	7.27	$-17.89^{+0.25}_{-0.27}$	$-2.37^{+0.04}_{-0.04}$
	136	7.20	$-17.40^{+0.15}_{-0.16}$	$-2.41^{+0.10}_{-0.10}$
*F*115*W* dropouts	37	9.31	$-19.99^{+0.37}_{-0.55}$	$-2.28^{+0.06}_{-0.07}$
	78	9.26	$-18.93^{+0.31}_{-0.39}$	$-2.33^{+0.09}_{-0.08}$
	117	9.31	$-17.98^{+0.42}_{-0.33}$	$-2.41^{+0.07}_{-0.07}$
*F*150*W* dropouts	24	12.02	$-18.61^{+0.81}_{-0.91}$	$-2.48^{+0.12}_{-0.14}$

the UV slopes of the *F*775*W* dropout sample appear to shift toward bluer β values at low UV luminosities, as been previously noted (e.g. Finkelstein et al. 2012; Bouwens et al. 2014; Bhatawdekar & Conselice 2021). We explore this trend by assigning objects in our sample to bins in M_{UV}, which are presented in Table 2. We find that the most UV-luminous galaxies at this redshift ($M_{UV} < -20$) display a median UV slope of $\beta = -2.12^{+0.06}_{-0.06}$, while the bin consisting of the faintest galaxies ($M_{UV} > -17.5$) has a median UV slope of $\beta = -2.38^{+0.12}_{-0.13}$. The number of galaxies at the redder end of the UV slope distribution ($\beta > -1.5$) appears constant as a function of M_{UV}. However, due to the increasing number of total galaxies, the fraction of $\beta > -1.5$ objects decrease toward low luminosities.

We quantify the observed trend between β and M_{UV} by fitting a linear relation to the median UV slopes for the luminosity bins of the
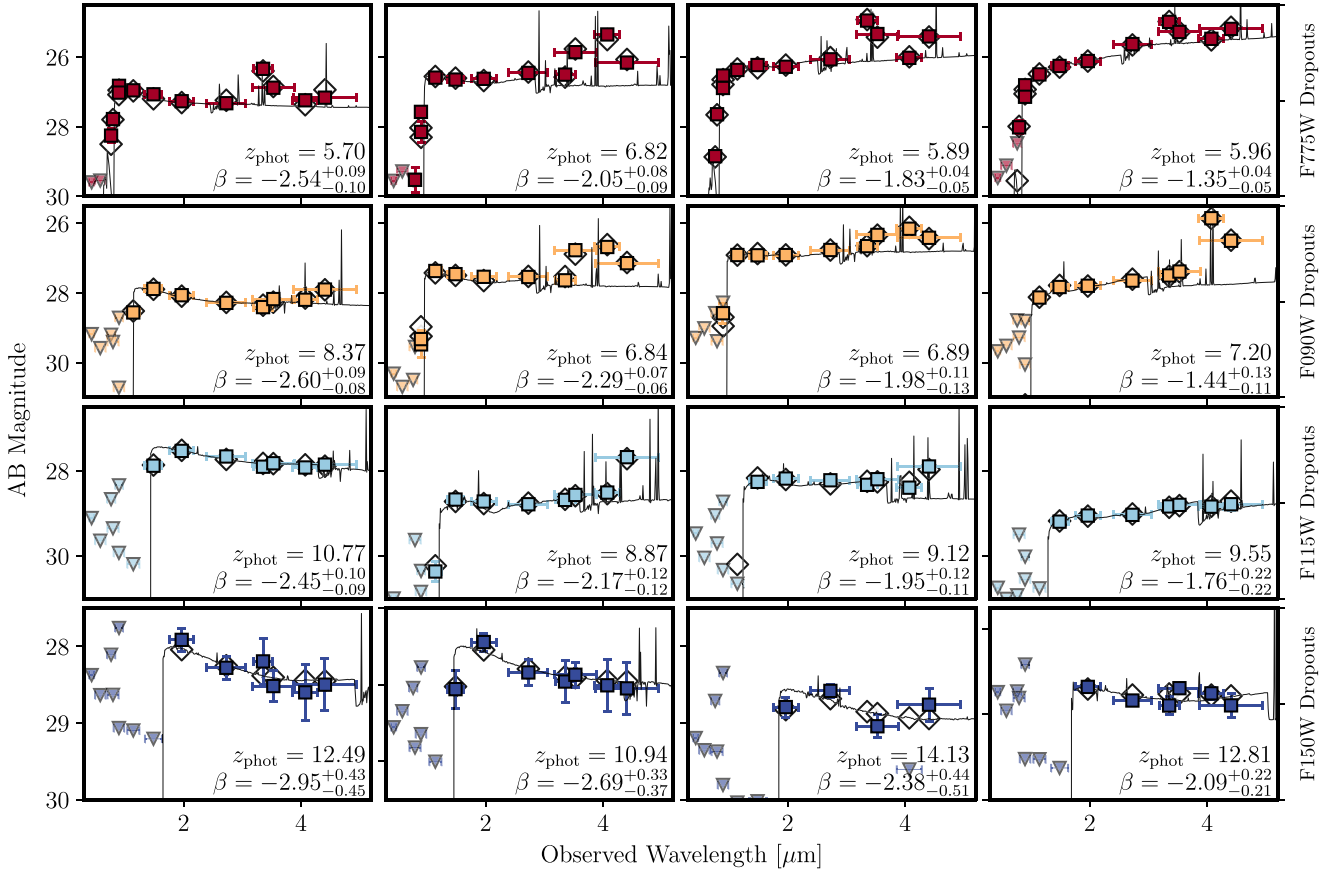
Figure 3. Example objects from each dropout selection, ordered from the lowest redshift sample (*F775W* dropouts; top row) to the highest redshift sample (*F150W* dropouts; bottom row), which are colour coded based on their dropout selection as in Fig. 1. Empty diamonds represent the photometric fluxes predicted by the best-fitting model, and coloured squares and triangles are measurements and upper limits, respectively. We display objects spanning a range of UV slopes within each selection, with bluer galaxies in the left column and redder galaxies in the right column. We list the measured UV slopes with uncertainties in addition to best-fitting photometric redshifts for each object.

Table 3. Best-fitting linear relations to UV slopes in bins of $M_{\rm UV}$. Uncertainties on the fit parameters are derived using a bootstrap Monte Carlo method described in Section 3. The intercept (β_0) listed here is calculated at an $M_{\rm UV} = -19$.

Sample	$z_{\rm phot}^{\rm med}$	$\mathrm{d}\beta/\mathrm{d}M_{\rm UV}$	β_0
F775W dropouts	5.86	-0.11 ± 0.02	-2.25 ± 0.03
F090W dropouts	7.28	-0.12 ± 0.02	-2.26 ± 0.03
F115W dropouts	9.41	-0.06 ± 0.05	-2.33 ± 0.05
F150W dropouts	12.02	-0.06 ± 0.05^a	-2.42 ± 0.13^a

[a] As the *F150W* dropout sample is composed of only one $M_{\rm UV}$ bin, we provide a fit assuming the slope is the same as our result for the *F115W* dropout sample.

form

$$\beta = \frac{\mathrm{d}\beta}{\mathrm{d}M_{\rm UV}} M_{\rm UV}^{-19} + \beta_0, \qquad (5)$$

where $M_{\rm UV}^{-19} \equiv M_{\rm UV} + 19$ and β_0 is the UV slope at an $M_{\rm UV} = -19$. The best-fitting parameters of this relation along with their uncertainties are presented in Table 3. We derive uncertainties on this best-fitting relation using a bootstrap Monte Carlo method, where we first construct a mock sample that matches the size and UV luminosity distribution of our observed sample, composed of objects

selected randomly from the observed sample with replacement. For each object in the mock sample, we perturb the rest-UV fluxes based on their uncertainties and measure the UV slope. We assign the resulting slopes to the same $M_{\rm UV}$ bins described above, and fit the binned median β using equation (5). This process is repeated 1000 times, and we take note of the linear fit parameters for each iteration. The uncertainties are then assigned as the range of the inner 68th percentile based on the resulting distribution.

This calculation reveals a significant correlation between β and $M_{\rm UV}$. We find a best-fitting slope of -0.11 ± 0.02 and normalization (defined at $M_{\rm UV} = -19$) of -2.25 ± 0.03, which is inconsistent with no correlation between β and $M_{\rm UV}$ at $>5\sigma$. Furthermore, a Spearman correlation test on the individual objects in the *F775W* dropout sample reveals a significant correlation, described by a correlation coefficient of $\rho_{\rm s} = -0.25$, with an associated probability of being drawn from an uncorrelated distribution of 1.4×10^{-6}. Using a sample of galaxies identified with *HST*, Bouwens et al. (2014) derive a trend between β and $M_{\rm UV}$ with a slope of -0.20 ± 0.04 for objects at $M_{\rm UV} = -22$ to -17, and a slope of -0.08 when just considering objects with luminosities fainter than $M_{\rm UV} > -18.8$. Together, these two estimates bracket the slope derived for our sample of *F775W* dropouts. We find that the fit to our data is well described by a single component, such that we find a consistent trend when only considering the three most UV-luminous bins. It is key to establish

this trend among luminous systems, as the low-luminosity population is more susceptible to selection biases (e.g. Dunlop et al. 2012; Rogers et al. 2013).

3.1.2 F090W dropouts

The total $F090W$ dropout sample ($6.5 \lesssim z \lesssim 8.5$) is characterized by a median $M_{UV} = -18.16$ and median UV slope of $\beta = -2.32^{+0.03}_{-0.02}$ (see Table 1). Nanayakkara et al. (2023) used *JWST* data to derive UV slopes for a sample of galaxies at a consistent redshift to our $F090W$ dropout sample. For their sample, they find a median UV slope of $\beta = -2.30 \pm 0.26$, which is in excellent agreement with our results. The UV slope distribution of the $F090W$ dropout sample provided in Fig. 2 appears qualitatively similar to that of the $F775W$ dropouts, though key differences are present. While the reddest sources at $z \lesssim 6$ approach values of $\beta \simeq -1$, the $F090W$ dropout sample contains no objects redder than $\beta > -1.4$. However, this does not represent a complete absence of moderately red ($\beta > -2.0$) sources. Two such examples are presented in Fig. 3, which have UV slopes of $\beta = -1.98$ and -1.44. Quantitatively, galaxies at $\beta > -1.5$ ($\beta > -1.2$) comprise a total of $9/656 = 1.3$ per cent ($0/656 = 0$ per cent) of the $F090W$ dropout sample, compared to $16/364 = 4.4$ per cent ($11/364 = 3.0$ per cent) of the $F775W$ comparison sample.

Galaxies with UV slopes bluer than $\beta < -2.5$ are present over a majority of the UV luminosity range sampled by the $F090W$ dropouts. The most luminous object in the sample with $\beta < -2.5$ is at $M_{UV} = -20$, and such objects persist down to $M_{UV} = -16.5$. The presence of these blue sources is in spite of the varying uncertainty in UV slopes, which are typically 0.03, 0.20, and 0.50, at an $M_{UV} = -21$, -19, and -17, respectively (see Fig. 2). This implies a significant width of the intrinsic UV slope distribution, hinting at variations in galaxy properties within the population at this epoch. While the typical β uncertainties grow large at low luminosities, many faint systems have UV slopes measured to much better precision, such as those falling within the deepest regions of the JADES footprint (Eisenstein et al. 2023). As we note below, these low-luminosity systems are crucial for our analysis of the population of extremely blue ($\beta \simeq -3$) galaxies.

We identify a clear trend between UV slope and M_{UV} with low-luminosity galaxies displaying bluer UV continua on average. We present the median UV slopes of these M_{UV} bins in Table 2, which are also displayed visually in Fig. 2. Following the same procedure outlined above, we fit a linear relation to the median β, and find a trend with a slope of -0.12 ± 0.02 that is normalized to a $\beta = -2.26 \pm 0.03$ at $M_{UV} = -19$. This relation supports the trend of bluer UV slopes toward lower luminosities with a significance in excess of 5σ. To explore variations of this trend as a function of M_{UV}, we fit a relation between each pair of bins, and in every case find a slope consistent with $d\beta/dM_{UV} = -0.12$. This suggests that the observed trend is consistent with a single-component relation. Previous studies have shown that faint galaxies with redder colours can be preferentially excluded due to photometric scatter, which biases the average UV slopes of the population to bluer values (e.g. Dunlop et al. 2012; Rogers et al. 2013). To address this, we simulate the UV slope distribution analytically by scattering the source photometry by their uncertainties and passing the results through our selections. We find only a minimal bias at the faint end of our sample, which is smaller than the uncertainties in the median UV slope presented in Table 2.

3.1.3 F115W dropouts

At $8.2 \lesssim z \lesssim 11.3$, the $F115W$ dropout sample ($z_{med} = 9.41$) displays a median UV slope of $\beta = -2.35^{+0.04}_{-0.04}$. The inner 68th percentile of

the UV slope distribution spans a range of β from -2.8 to -1.9, notably shifted toward bluer UV slopes when compared to the lower redshift samples. We present several examples of objects in our $F115W$ dropout sample in Fig. 3, where galaxies with UV slopes ranging from $\beta = -2.5$ to -1.7 are shown. Among the full $F115W$ dropout sample, only five objects display UV slopes redder than $\beta = -1.5$, with the reddest galaxy displaying a UV slope of $\beta = -1.31$. We find objects fitting this moderately red ($\beta > -1.5$) criteria at $M_{UV} = -21$ as well as at $M_{UV} = -17$. However, the majority of the reddest sources (four out of five) have absolute magnitudes placing them in the most luminous half of the sample ($M_{UV} < -18.24$).

We divide the $F115W$ dropout sample into bins of M_{UV} to explore the trend between UV slope and UV luminosity. Due to the number of $F115W$ dropouts, we divide the sample into three bins, with median M_{UV} of $-19.99^{+0.37}_{-0.55}$, $-18.93^{+0.31}_{-0.39}$, and $-17.98^{+0.42}_{-0.33}$. The median UV slopes of each bin are provided in Table 2, with uncertainties derived using the same bootstrap Monte Carlo method described above. As with the lower redshift samples, the median UV slopes of the $F115W$ dropouts become increasingly blue at the faint end of the sample. Specifically, we find a UV slope of $\beta = -2.28^{+0.06}_{-0.07}$ for the most UV-luminous bin at $M_{UV} = -19.99$, trending to $\beta = -2.41^{+0.10}_{-0.10}$ at $M_{UV} = -17.98$. We fit a linear relation to these bins and find a best-fitting relation of $\beta = (-0.06 \pm 0.05)(M_{UV} + 19) + (-2.33 \pm 0.05)$. Notably, the resulting best-fitting relation is decidedly shallower than those of the lower redshift $F775W$ and $F090W$ dropout samples.

A driving factor in this shallow slope is the blue colour of the most UV-luminous galaxies in our sample. As noted above, this stems mostly from the dearth of moderately reddened ($-2.0 < \beta < -1.5$) objects at high UV luminosities in the $F115W$ dropout sample. Excluding the bin at $M_{UV} \simeq -20$ from the linear fit reveals a much steeper trend with β, characterized by the relation $\beta = -0.09 \times (M_{UV} + 19) - 2.33$. Given this relation, we would expect the median UV slope of the most luminous bin to be $\beta = -2.24$, which is within the uncertainty of the observed median. One possible cause for this difference among bright galaxies results from the relatively small sample size of the brightest bin. In contrast, the intermediate UV luminosity bin has over double the sample size, which contains 18 galaxies within the UV slope range $-2.0 < \beta < -1.5$. If a consistent fraction were present among the brightest bin, we would expect eight such galaxies in the most UV-luminous bin.

3.1.4 F150W dropouts

The $F150W$ dropout sample includes the highest redshift objects analysed in this work, comprising 24 galaxies spanning $11 < z_{phot} < 14$. A majority (20) of the objects satisfying these selection criteria have already been presented in Hainline et al. (2023), and the remaining four objects (that are very faint) will be discussed further in Whitler et al. (in preparation). Due to the small number of galaxies falling into this selection, and the relatively narrow range of M_{UV} spanned by the sample, we are unable to construct multiple bins of M_{UV}. Thus, we explore the $F150W$ dropout sample as a whole, finding a median M_{UV} of $-18.61^{+0.81}_{-0.91}$ along with a median redshift of $z_{phot} = 12.02$ (see Table 1). At the redshifts probed by this sample, the rest-optical emission from galaxies has redshifted beyond wavelengths probed by *JWST*/NIRCam, making UV slopes one of the few remaining observational probes of galaxy properties. For this $F150W$ dropout sample, we find a median UV slope of $\beta = -2.48^{+0.12}_{-0.14}$. We present several examples of objects selected as $F150W$ dropouts in Fig. 3, illustrating the variety of β observed in this sample despite the relatively small sample size.
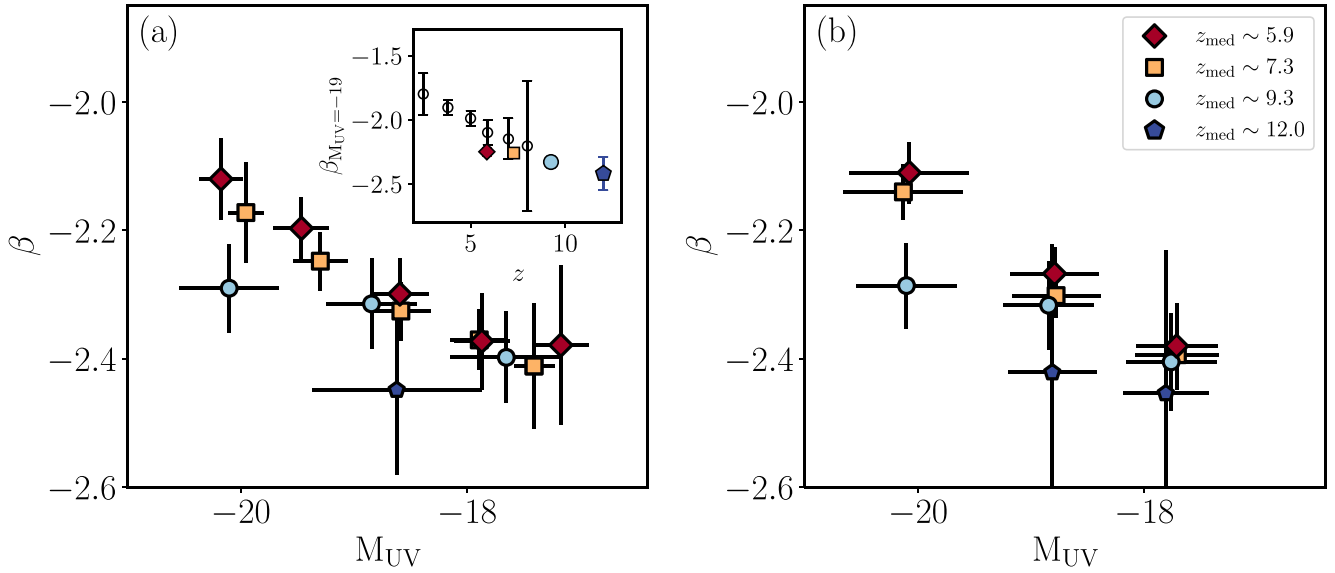
Figure 4. UV continuum slope, β, displayed as a function of M_{UV} for the four dropout samples described in Section 2.2. (a) Each sample is divided into bins of M_{UV}, with the exception of the *F150W* dropout sample median, which comprises the entire selection. For each sample explored in multiple bins of M_{UV}, we observe a clear trend with β such that fainter galaxies typically have bluer UV slopes. While this trend is clear throughout the different samples, the overall normalization decreases with increasing redshift. At fixed M_{UV} the median UV slopes trend toward bluer values. The inset panel illustrates the median UV slope calculated at an $M_{UV} = -19$ for our four dropout samples compared to the results from Bouwens et al. (2014) represented by small open circles. (b) Median UV slopes for each sample derived using a fixed set of M_{UV} bins. We find similar trends when using consistent M_{UV} bins to when each redshift sample is delineated into different bins of UV luminosity, such that the most UV-luminous galaxies exhibit a larger evolution at $z > 9$. Each median UV slope derived for the *F150W* dropout sample comprises only $\sim$10 galaxies, resulting in the large uncertainties displayed here.

Strikingly, the *F150W* dropout sample constitutes an epoch where we observe the disappearance of a significant portion of the sample with $\beta \gtrsim -2.0$. We test our ability to identify such sources by artificially scattering the photometry of our sample by their uncertainties such that they fall into this moderately red regime. This investigation reveals that we do recover these galaxies, suggesting that the lack of a $\beta \gtrsim -2.0$ population is not driven by selection effects. While we have described some differences in the abundance of such sources among our lower redshift samples, the *F150W* dropouts are markedly distinct in this regime. Such systems comprise 22.8, 17.5, and 19.4 per cent of objects among our samples at $z_{phot} =$ 5.86, 7.28, and 9.41, respectively. Adopting a similar fraction for the *F150W* dropout sample, we may expect $\sim$5 of these objects to have been selected in our sample. While only one such object has found its way into the selection, larger samples of galaxies in this redshift range may reveal better consistency with the lower redshift samples, or confirm the dearth of moderately red galaxies at the earliest epochs.

As the number of *F150W* objects in our sample is small, we are not able to place meaningful constraints on the M_{UV} dependence of the UV slopes. However, we explore the trend that may exist if we make an assumption on the slope of the relation. Specifically, if we adopt the slope derived from the *F115W* dropouts (i.e. $d\beta/dM_{UV} = -0.06$), the normalization provided by the median *F150W* dropout slope yields a relation of $\beta = -0.06(M_{UV} + 19) - 2.42$. We provide the parameters of this fit in Table 3, but note that it was derived assuming a slope fixed to that of the *F115W* dropouts. If instead we adopt the steeper slope found for the *F090W* dropouts (e.g. $d\beta/dM_{UV} = -0.12$), we achieve a relation of $\beta = -0.12(M_{UV} + 19) - 2.43$. These two relations make substantially different predictions when extrapolated to values of M_{UV} beyond the extent spanned by the

sample. Specifically, at an M_{UV} of -20, the steeper of these relations predicts a β of -2.31, which would be consistent with the UV-bright *F115W* dropouts, while the shallower of these relations would yield a $\beta = -2.37$. Larger samples that can expand the dynamic range of M_{UV} probed in this epoch will unveil any UV luminosity dependence of β among this population.

3.2 Redshift evolution of typical UV slopes from $z = 6$–12

The typical UV slopes derived for the four dropout samples demonstrate a key aspect of evolution in galaxy properties at $z \gtrsim 6$. The redshift evolution is apparent in Fig. 4(a) where the median UV slopes become more blue toward higher redshift at fixed M_{UV}. At an $M_{UV} = -19$ (which is well sampled by each of our dropout samples), we find a shift in the typical UV slopes from $\beta = -2.25$ at $z \sim 6$ to a $\beta = -2.42$ at $z \sim 12$. The results for each of our samples are presented in the inset panel of Fig. 4. We quantify the strength of this trend by fitting a linear relation to these medians, and find that they imply a redshift evolution with β at a rate of $d\beta/dz = -0.030^{+0.024}_{-0.029}$.

This derived evolution provides an extension upon previous results finding a similar trend among lower redshift samples (e.g. Bouwens et al. 2012, 2014; Finkelstein et al. 2012). Up to $z \sim$ 6, Bouwens et al. (2014) derive a UV slope evolution of $d\beta/dz = -0.10 \pm 0.06$, which is broadly consistent with the evolution derived from our *JWST* sample. The median UV slope from our $z \sim 6$ (corresponding to *F775W* dropouts) sample lies roughly 1σ below the Bouwens et al. (2014) measurement at the same redshift. This slight discrepancy is one element causing our estimate of the redshift evolution to be slower than what has been found by Bouwens et al. (2014). For redshifts of $6 \lesssim z \lesssim 8$ (i.e. where the two samples overlap), we find good consistency between the median

UV slopes. At yet higher redshift, our results are in agreement with the typical UV slopes obtained when extrapolating the Bouwens et al. (2014) trend to earlier times. Using just these objects in our sample ($z > 8$), we measure an evolution of $d\beta/dz = -0.07^{+0.05}_{-0.06}$, consistent with the trend derived at lower redshift in Bouwens et al. (2014).

The JADES results suggest the evolution in UV colours proceeds differently at different UV luminosities. We find significantly faster evolution toward bluer colours at $M_{UV} = -20$ than at $M_{UV} = -18$, amounting to a $d\beta/dz = -0.038 \pm 0.017$ and $d\beta/dz = -0.008 \pm 0.017$, respectively. As is clear in Fig. 4(a), the lowest luminosity galaxies in our sample show minimal evolution between $z \simeq 6$ and $z \simeq 9$. This may reflect a larger fraction of the lower luminosity population approaching the intrinsic values expected for normal stellar populations in the absence of dust by $z \simeq 6$, thereby saturating the blueward evolution (Cullen et al. 2017). In contrast, the most luminous galaxies in our sample show marked evolution between $z \simeq 7$ and $z \simeq 9$, with very blue slopes ($\beta = -2.3$) becoming typical for $M_{UV} = -20$ at $z \simeq 9$. This may suggest rapid evolution in the dust content of the most UV-luminous galaxies, an effect that has been noted as a possibility to address the high number of UV-luminous systems appearing at $z > 10$ (e.g. Ferrara, Pallottini & Dayal 2023; Mason, Trenti & Treu 2023). In addition, larger fractions of a population approaching this intrinsic limit ensures that several prerequisites (e.g. no dust) are in place that allow for extreme UV slopes (e.g. $\beta \simeq -3$) to exist in greater abundance. We describe such objects within our sample in detail in the following section.

While we have thus far chosen different UV luminosity bins at each redshift reflecting their sample sizes and demographics, we now consider evolution within fixed M_{UV} bins. We assemble each sample into the M_{UV} bins previously defined for the *F115W* dropouts, and display the results in Fig. 4(b). The trends with both redshift and UV luminosity seen using this alternative binning scheme are consistent with the trends derived when each sample is binned distinctly. Specifically, among the fixed M_{UV} bins we find that the most UV-luminous objects ($M_{UV} = -20$) display the largest change in their average UV slopes between $z \simeq 7$ and $z \simeq 9$ ($\Delta\beta = 0.09$). However, the less UV-luminous bins at $M_{UV} \simeq -19$ and -18 show only minimal evolution ($\Delta\beta = 0.02$). This supports our previous result that the UV-faint population may comprise a large percentage of galaxies near the intrinsic limit UV slope limit, leaving little room for bulk evolution.

The UV slope evolution described in this section demonstrates that galaxies at $z \gtrsim 9$ are unmistakably blue on average. At $z \sim 9.3$ and $z \sim 12.0$ we find median UV slopes of $\beta = -2.33^{+0.09}_{-0.08}$ and $\beta = -2.48^{+0.12}_{-0.14}$, implying evolution continues to the highest redshifts. The ubiquity of blue colours in galaxies at these epochs is also present within semi-analytic galaxy evolution models (e.g. Mirocha & Furlanetto 2023; Yung et al. 2024), driven by a range of physical effects (e.g. dust attenuation and stochasticity of star formation). Mirocha & Furlanetto (2023) utilized these theoretical models to explore the processes that drive the apparent overabundance of UV-bright sources at early times. In doing so, they find that galaxies with UV slopes of $\beta \simeq -2.0$ to -2.5 are typical at $z > 8$, in agreement with our results. However, the physical processes imposed in the models of Mirocha & Furlanetto (2023) may not be the only way to reproduce observed galaxy abundances. Additional insight into the evolving UV slope distribution, such as the absence of moderately red sources at $z \sim 12$ noted in this work, will provide significant leverage to inform future models of galaxy evolution.

4 GALAXIES WITH VERY BLUE UV SLOPES IN JADES

We now investigate the bluest galaxies in the JADES data base at $z \gtrsim 6$ with UV slopes approaching $\beta \simeq -3$. Interest in this population is driven by their potential for indicating LyC photon leakage or exotic stellar populations (e.g. Bouwens et al. 2010; Ono et al. 2010; Robertson et al. 2010; Zackrisson et al. 2013; Jiang et al. 2020; Topping et al. 2022; Cullen et al. 2023). In this section, we first identify our most stringent population of very blue galaxies (Section 4.1) before exploring their properties (Section 4.2) and discussing the potential impact of bursty SFHs on the observed colours (Section 4.3).

4.1 A population of extremely blue UV objects at $z \gtrsim 6$

As is clear from Fig. 2, a significant subset of the 1276 galaxies in our dropout samples have observed UV slopes nearing $\beta = -3$. Our first goal in this section is to identify those galaxies that are most likely to have very blue UV slopes. We find that 14 per cent (184) of objects across the full sample have UV slopes of $\beta < -2.8$. In this regime, standard population synthesis models struggle to explain the colours with ionization-bounded interstellar medium conditions. However interpretation of such blue galaxies has long been impacted by photometric uncertainties, as the error on β is often large enough such that the blue UV slopes can be the result of anomalous scattering.

We seek to identify the subset of very blue ($\beta < -2.8$) sources that are most robust against concerns of photometric scatter. To achieve this goal, we first require that the uncertainty on the UV slope is small enough ($\sigma_\beta < 0.3$) to minimize the inclusion of very noisy sources likely to have significant scatter in their β measurements (see also Cullen et al. 2023 for an alternative approach). This reduces the very blue sample to 62 objects. Following Topping et al. (2022), we fit this sample with density-bounded templates (Plat et al. 2019) that allow UV slopes to approach the very blue values ($\beta \simeq -3.2$) observed in this sample. These models allow for nebular emission to be self-consistently computed while allowing for the escape of ionizing photons in the density-bounded regime. The density-bounded models generally result in good fits to the observed SEDs, making significant improvements with respect to the standard ionization-bounded models. This is clearly seen in the SEDs shown in Fig. 5, with χ^2_ν improving from 0.5–12.1 (median 2.2) in the $f_{esc} = 0$ models to 0.3–9.7 (median 1.8) when $f_{esc} > 0$ models are allowed (Fig. 5f).

In some cases, we see that the observed blue UV slopes may be significantly influenced by one photometric filter that is offset from the SED. For example, if the observed flux in the filter just redward of the Lyα break is well in excess of the SED (owing to photometric scatter), it can lead to an anomalously blue UV slope. We conservatively excise such objects from the sample. To identify these sources, we select galaxies where the observed flux density in one or more of the rest-UV filters is significantly offset from the best-fitting density-bounded models (i.e. by more than the photometric uncertainty in that filter). With this cut, our extremely blue sample reduces to 44 galaxies, comprising 3.4 per cent of our total sample. Of these 44 galaxies, 14, 19, and 11 objects are in the *F775W*, *F090W*, and *F115W* selections, respectively. We present the SEDs for each object in this sample in Fig. 6. Following the cleaning of this very blue sample we find an overall improvement to the χ^2_ν from the model fits, which range from 0.3 to 6.1 (median 1.7). This extremely blue sample spans a range of redshifts from $z_{phot} = 5.42$ to 10.96 ($z_{med} = 7.18$) and UV luminosities corresponding to $M_{UV} = -19.7$ to -17.2
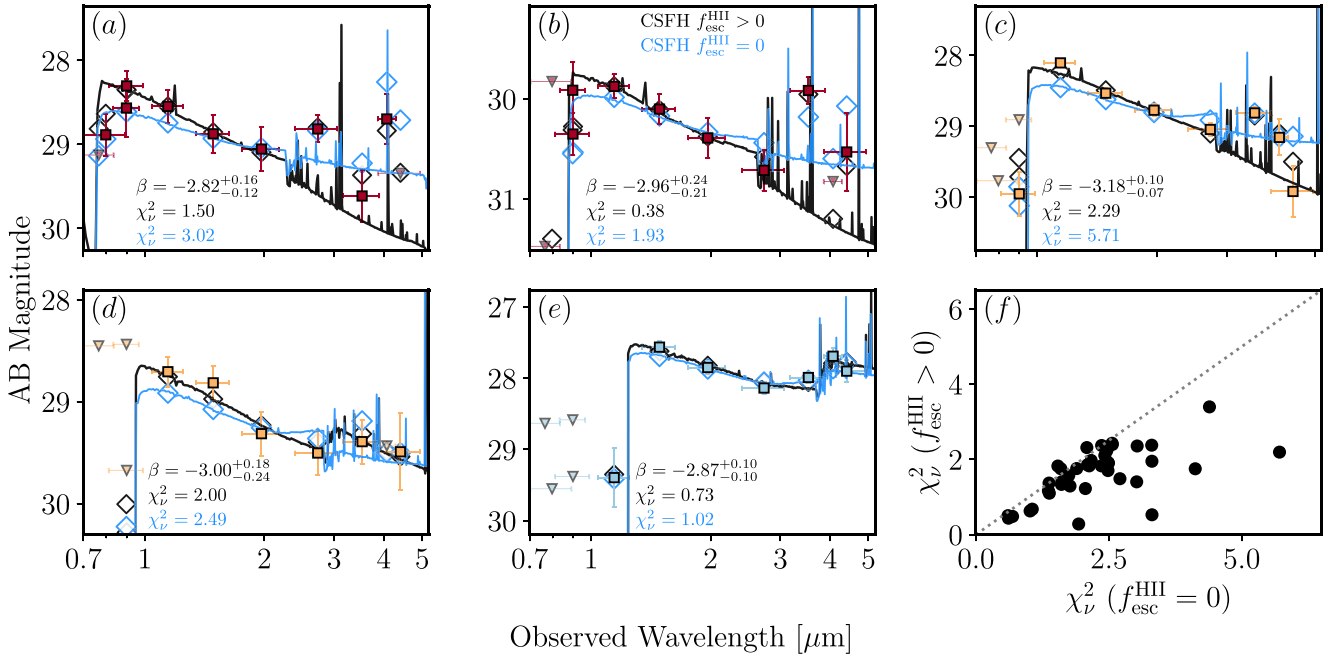
Figure 5. Demonstration of improved fit quality when templates with $f_{esc} > 0$ are used to model the photometry of our extremely blue sample. Panels (a)–(e) show the best-fitting SED models derived assuming $f_{esc} = 0$ in blue, while the models allowing for high f_{esc} are shown in black. Photometry is colour coded based on their dropout sample as defined in Fig. 1. We list the reduced χ^2 for both of these model fits in each panel. Panel (f) directly compares the reduced χ^2 between the two model fits for the entire extremely blue sample. In nearly all cases, allowing for high values of f_{esc} yields a much better fit, indicated by the lower χ^2.

(median $M_{UV} = -18.0$). The UV slopes span from $\beta = -2.81$ to -3.26 ($\beta_{med} = -2.95$), with typical uncertainties of 0.23, much less than the typical uncertainties found for galaxies in our full sample at these M_{UV} (e.g. 0.43 at $M_{UV} = -18$; Section 3.1). The density-bounded models require fairly large escape fractions to match the observed SEDs (median $f_{esc} = 0.51^{+0.08}_{-0.09}$), with the highest f_{esc} in the sample reaching 0.86. A small fraction of this sample (6/44) have inferred f_{esc} of less than 20 per cent. This small number of objects with lower f_{esc} typically have UV slopes near the edge of the selection (i.e. $\beta \simeq -2.8$).

Having identified a small sample of galaxies with very blue UV colours, we now more closely investigate the impact of photometric scatter on our measured colours. We are in particular interested in determining if photometric uncertainties are expected to scatter significantly more sources into the extremely blue regime ($\beta < -2.8$) than are observed. We quantify the number of sources expected to scatter to very blue colours using a simple set of simulations that mock-up galaxies with the same demographics as those found for this analysis (see Section 2.2). This mock sample is constructed independently for each of the dropout samples described above. We randomly select a UV luminosity from the M_{UV} distributions presented in Section 2.2. From this UV luminosity, we assign a UV slope based on the relations in Section 3.1, to which we apply a scatter of 0.2, consistent with the spread of β found for objects at the bright end of our sample where photometric scatter is minimal (and the observed scatter is assumed to be intrinsic). Based on the selected M_{UV} and assigned β, we derive mock photometry in filters sampling the rest-frame UV. We next assign flux uncertainties to the mock SEDs. The uncertainties are randomly selected from our observed sample for objects that are matched in M_{UV}, naturally approximating the varying observing depths across the JADES mosaics (Eisenstein et al. 2023). We perturb the mock photometry by

their assigned uncertainties, and measure the UV slope as described in Section 2.3. This process is repeated until the mock sample contains the same number of objects as each observed dropout sample.

We present a typical realization of these simulations in Fig. 7. As expected, the observed scatter of UV slopes for this mock sample increases greatly at low UV luminosities. By passing the mock samples through our criteria for robust extremely blue sources, we can estimate the number of objects expected to exist due to scatter. At all UV luminosities, these simulations underpredict the number of robust extremely blue sources. The robust extremely blue objects comprise 2.0, 3.2, and 4.5 per cent of the observed sample at $-20 \leq M_{UV} < -19, -19 \leq M_{UV} < -18$, and $-18 \leq M_{UV} < -17$, respectively, while the robust objects in these simulations yield only 0, 1.6, and 2.6 per cent, in the same UV luminosity bins. In total, scattering these galaxies to blue UV slopes yields less than half of the number of robust objects of our observed sample (32 per cent on average), implying that photometric scatter alone cannot explain the observed sample of extremely blue objects with our adopted assumptions on intrinsic scatter. This analysis has primarily focused on the rest-UV measurements, while in the following section, we determine if the extremely blue UV slopes are supported by the rest-optical SEDs.

4.2 Physical properties of galaxies with very blue UV slopes

In the previous section, we assembled a sample of $z \gtrsim 6$ galaxies in the JADES footprint with very blue colours ($\beta < -2.8$). We demonstrated that density-bounded photoionization models (Plat et al. 2019) can successfully reproduce the SEDs with a typical escape fraction of $f_{esc} = 0.51$. Here we begin to investigate the physical properties of the sources. We first explore the rest-
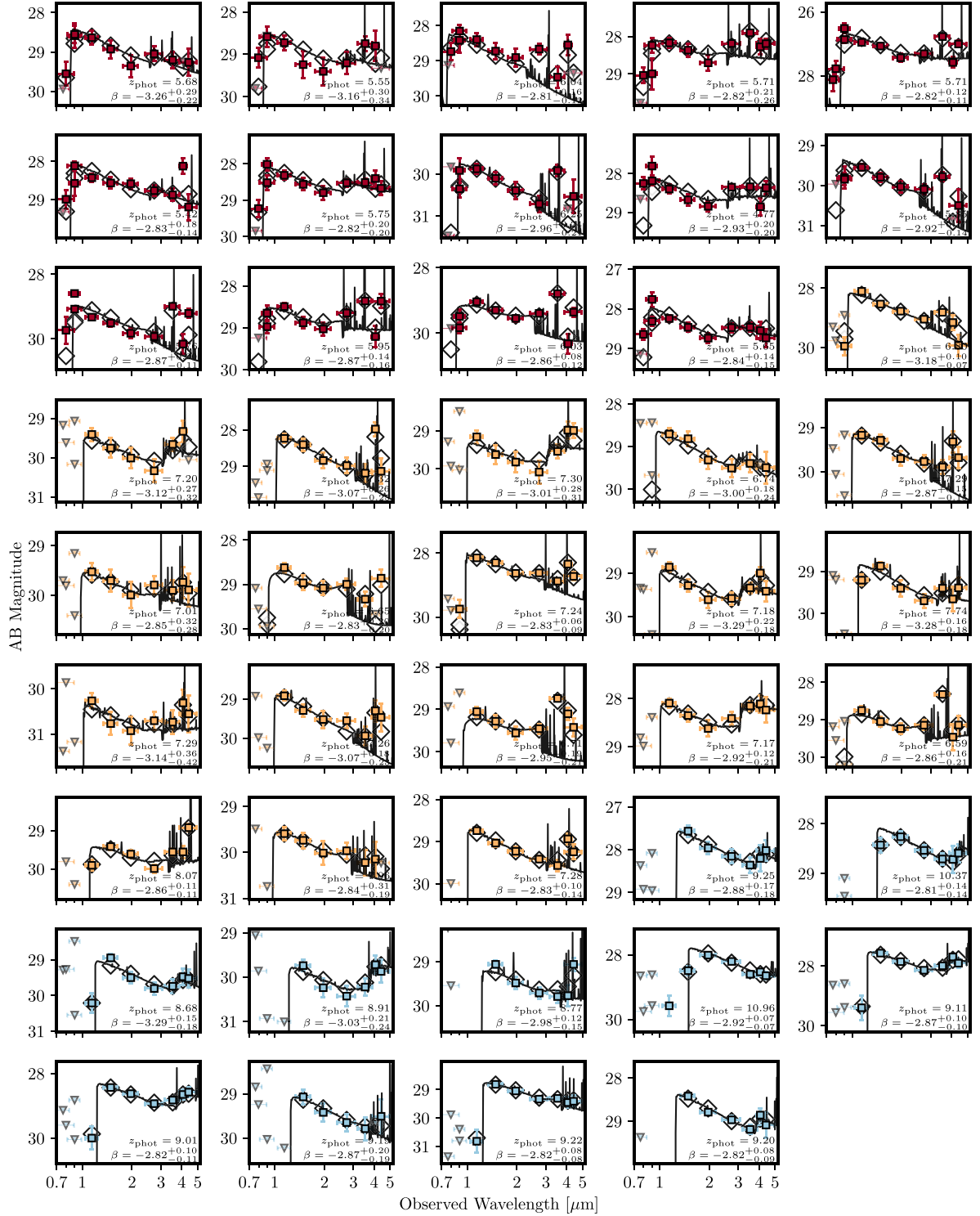
Figure 6. Best-fitting SEDs for galaxies with extremely blue UV slopes discussed in Section 4.1. In each panel, we display the photometric redshift and UV slope along with their uncertainties. The observed fluxes are displayed according to the sample from which the objects were derived, such that *F*775*W*, *F*090*W*, and *F*115*W* dropouts are displayed as red diamonds, orange squares, and blue circles, respectively.

optical SEDs, paying particular attention to the emission line strengths. We then investigate whether the properties implied by the SEDs are distinct from the general population and compare the SFR surface densities to the known population of LyC leakers.

If the very blue galaxies are leaking a large fraction of their ionizing radiation, we would expect their rest-optical emission lines to be significantly weakened (e.g. Zackrisson et al. 2013). The influence of these emission lines is readily seen in flux excesses in medium- and broad-band NIRCam filters (e.g. Endsley et al. 2023b). Using
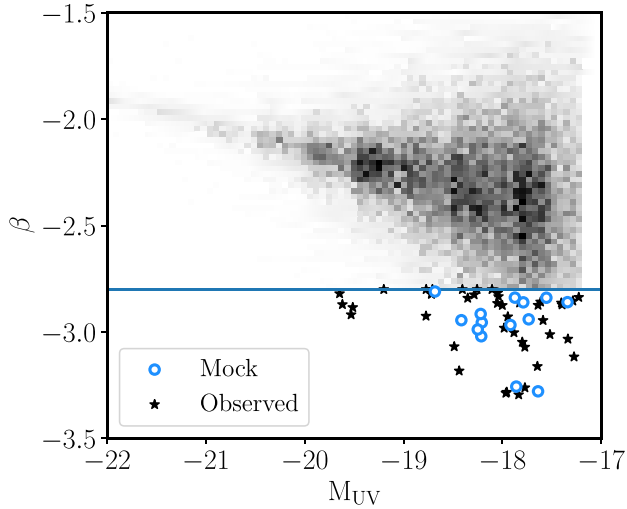
Figure 7. Simulated UV slope distribution constructed from the measured intrinsic relation between β and $M_{\rm UV}$ with simulated scatter derived from the photometric flux uncertainties. The mock sample is designed to have demographics matching that of our observed sample as described in Section 2.2. We indicate the $\beta = -2.8$ threshold for considering an object as extremely blue with a horizontal line. Despite a fixed intrinsic width of the UV slope distribution, the decreasing signal-to-noise ratio measured for fainter systems results in a significant increase in the observed β scatter. We impose our criteria for robust extremely blue objects described in Section 4.1, and display the resulting sample as blue circles. For comparison, we plot our observed sample of robust extremely blue objects as black stars. It is clear that while photometric scatter is capable of producing galaxies that fall into our robust selection, it appears to not be able to explain the observed sample, both in number and in UV luminosity range.

the JADES filters, the LW colours are sensitive to the [O III] + Hβ equivalent widths (EWs) within two redshift windows. Within $5.9 < z < 6.6$ ($7.1 < z < 8.9$), the [O III] + Hβ lines fall in the $F356W$ ($F444W$) filter, while the $F410M$ ($F356W$) filter is sensitive to the continuum only.

We compare the observed UV slopes and LW colours of the extremely blue sample to models of density-bounded H II regions. For this comparison, we construct a grid of models using templates from Plat et al. (2019) for values of $f_{\rm esc}$ from 0 to 1 in steps of 0.25, in addition to a broad range of ages (1–400 Myr) and metallicities ($\log(Z/Z_\odot) = -2$ to 0) in steps of 0.1 dex. We present the colours and UV slopes derived from these models in Fig. 8. These models illustrate two clear characteristics: higher values of $f_{\rm esc}$ allow models to achieve bluer UV slopes, and at bluer UV slopes the colour excesses (i.e. emission line EWs) are weaker (e.g. Zackrisson et al. 2013; Topping et al. 2022). We define the following regions of the colour–β space that encompass the model predictions at $\beta < -2.8$ and corresponding to high $f_{\rm esc}$ (> 50 per cent):

$$\begin{cases} \beta < -2.8, \\ F410M - F356W > -0.1, \\ F410M - F356W < 1.67 \times \beta + 6.16 \end{cases} \quad (6)$$

for galaxies within the redshift range $5.7 < z < 6.5$, and

$$\begin{cases} \beta < -2.8, \\ F356W - F444W > -0.4, \\ F356W - F444W < 1.67 \times \beta + 5.67 \end{cases} \quad (7)$$

for galaxies at $7.1 < z < 8.9$. These two regions are highlighted in Fig. 8.

The colours and UV slopes of our extremely blue sample are also compared to these regions in Fig. 8. In total, 22 (50 per cent) galaxies from our extremely blue sample fall within the redshift ranges described above. This figure illustrates that nearly all galaxies within this redshift-restricted subsample (16/22) fall within the β–colour space informed by the models. The remaining six objects are slightly outside the boundary of these two regions; however, they are consistent within the uncertainties. It is clear that the bluest subset ($\beta < -3.0$) of our $\beta < -2.8$ sample possesses the weakest rest-optical colour excesses. We find a median $m_{F356W} - m_{F444W}$ colour for this bluest subset of 0.11 mag, while typical colours of objects with $-2.8 < \beta < -3.0$ are elevated to 0.27 mag. These colours imply [O III] + Hβ EWs of 221 and 317 Å for the $\beta < -3.0$ and $-2.8 < \beta < -3.0$ subsamples, respectively. The comparatively weak lines inferred for these sources provide a key self-consistent check on expectations from models with high $f_{\rm esc}$.

We explore the rest-optical emission lines further in Fig. 9. Here we compare the colour excesses of our extremely blue objects to a representative sample of galaxies pulled from the selection in Section 2.2. First concentrating on the subsample of objects $7.1 < z < 8.9$, we find a median $F356W - F444W$ colour for the extremely blue objects of 0.19 mag, which is systematically lower than the 0.39 mag found for the full sample. This difference is reflected in the [O III] + Hβ EWs; the extremely blue objects are characterized by a median EW of 256 Å, which are systematically weaker than the 340–780 Å expected for typical galaxies in this epoch (Endsley et al. 2023b). It is conceivable that the extremely blue galaxies lie at redshifts where the observed-frame wavelengths of [O III] + Hβ lines correspond to low-throughput regions of the filter sensitivity curves. In turn, this would cause the emission lines to be less effective at producing colour excesses. To explore this possibility, we display the $F356W - F410M$ colours as a function of photometric redshift in Fig. 9(b). For this test, we use the narrower $F410M$ filter, as it is more sensitive to the presence of emission lines, however, over a smaller redshift range. Throughout the redshift range where [O III] + Hβ contributes to the $F410M$ flux, the extremely blue sample yields LW colours implying emission lines that are weaker than the full sample on average. The median $F356W - F410M$ colour of the full sample reaches its maximum at a redshift of $z \simeq 7.3$ and has a value of 1 mag. Extremely blue objects at the same redshift are all below this value, have a maximum colour of 0.6 mag, and primarily fall into the range of 0.3–0.5 mag. This provides additional evidence that the extremely blue sample displays systematically weaker emission lines than the overall galaxy population, in agreement with their leaking of significant ionizing radiation.

Fig. 10 presents SEDs for a subset of our extremely blue sample that appear to have weak emission lines. Each object displayed here lies at $z < 8.9$, such that the [O III] + Hβ lines fall within the NIRCam filters. While a visual inspection of these SEDs already indicates the absence of strong emission lines, the full SED modelling of their photometry confirms that the emission lines are very weak, with BEAGLE-derived EWs of only 200–250 Å. In combination, extremely blue UV slopes and weak rest-optical emission lines provide a compelling case for high $f_{\rm esc}$ among these galaxies. We note that weak emission lines are not uniquely caused by high $f_{\rm esc}$; however, the alternative solutions such as extremely low metallicities or complex SFHs (see Endsley et al. 2023b) yield different predictions for the overall SED. For example, extremely low metallicities would result in a strong nebular continuum component of the emission, making UV slopes of $\beta < -2.8$ impossible. In contrast, complex SFHs may be able to reproduce the observed SEDs, which we discuss in detail in the following section.
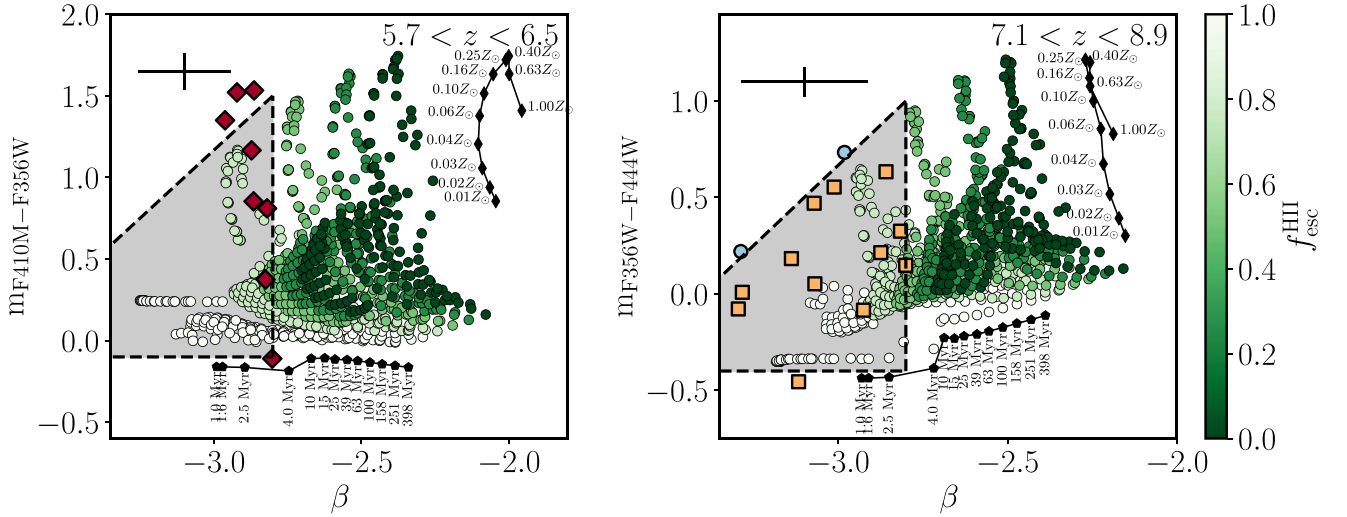
Figure 8. Inferred emission line strengths of the extremely blue sample. The left panel shows the selection at redshifts of $5.7 < z < 6.5$, while the right panel is for $7.1 < z < 8.9$. In each panel, we display colours and UV slopes calculated from model templates for five values of f_{esc}, and over grids of metallicity ($\log(Z/Z_\odot) \in [-2, 0]$) and age ($\log(\mathrm{Age/yr}) \in [6, 9]$) as the green points. The labelled black diamonds and pentagons demonstrate how the model points vary at fixed age and metallicity, respectively. Galaxies within our sample selected as *F775W*, *F090W*, and *F115W* dropouts are displayed as red diamonds, orange squares, and blue circles, respectively. The shaded region enclosed by black dashed lines indicates our selection of robust objects with extremely blue UV slopes and relatively weak lines. We provide the median error bars in the top left of each panel.
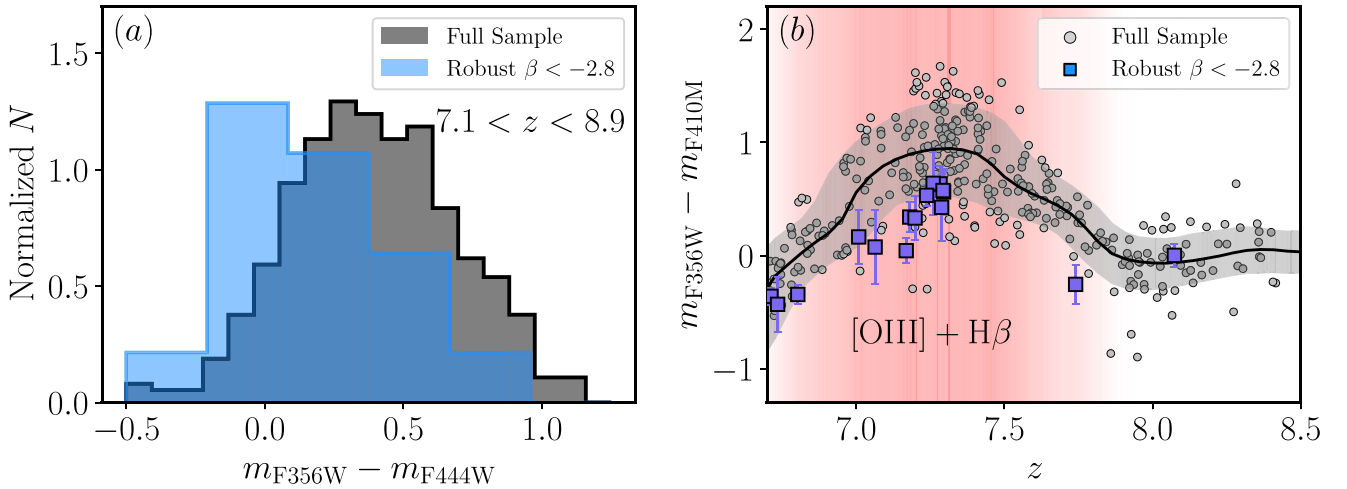
Figure 9. Comparison between colour excesses of the extremely blue galaxies and the full dropout samples. (a) $F356W - F444W$ colour distribution for galaxies with photometric redshifts at $7.1 < z < 8.9$, where this LW colour is sensitive to the [O III] + Hβ EW. We present colours for the full sample in the grey histogram, which has a median value of 0.39 mag. In comparison, we show colours from galaxies in our extremely blue sample in the blue histogram with a median value of 0.19 mag implying weaker emission lines compared to the full sample. (b) $F410M$ narrow-band excess as a function of redshift for the full sample (grey points) and the extremely blue objects (blue points). At $7.0 \lesssim z \lesssim 7.5$, [O III] + H$\beta$ contributes to the $F410M$ flux, resulting in a colour excess (red shaded region). These colours imply that the extremely blue galaxies have weaker lines at fixed redshift than the full sample on average.

We next explore the SED-based properties of this candidate population of high-f_{esc} systems. Previous analyses have argued using both observational (e.g. Heckman et al. 2011) and theoretical work (e.g. Rosdahl et al. 2022) that intense feedback can drive high escape fractions, with such feedback being particularly significant among young, high specific star formation rate (sSFR) galaxies. These characteristics are common among our extremely blue sample that is typically young (median CSFH age $14.8^{+9.8}_{-5.8}$ Myr), with an average sSFR of 79 Gyr^{-1}. This sSFR is nearly a factor of 2 greater than the median found for the full sample (44 Gyr^{-1}). In a similar

manner, much debate has centred on whether higher escape fractions are more prevalent among lower or higher stellar mass galaxies (e.g. Ma et al. 2020; Naidu et al. 2020; Saldana-Lopez et al. 2023) due to the interplay of star formation, galaxy geometry, and dust attenuation (see e.g. Pahl et al. 2023 for a discussion). We find that all of the objects in our extremely blue sample have masses in the range $\log(M/M_\odot) = 7.0$–8.5, with a median of $\log(M/M_\odot) = 7.5^{+0.2}_{-0.2}$, consistent with the range of stellar masses where f_{esc} is highest on average, based on the cosmological simulations of Ma et al. (2020). However, we note that selecting sources with high f_{esc} based on
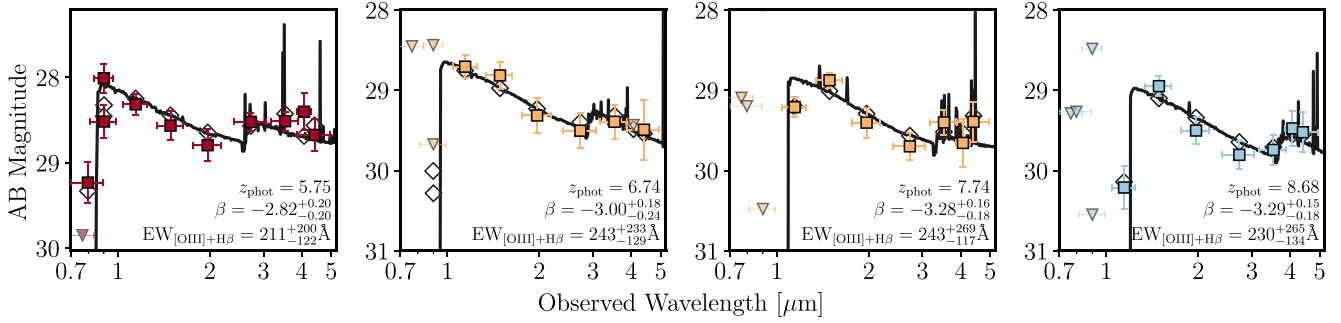
Figure 10. Examples of galaxies in our extremely blue sample that display no significant photometric excesses, implying weak rest-optical emission lines. In each panel, we present the UV slope measured from the photometry, and photometric redshift and [O III] + Hβ EW inferred from the best-fitting BEAGLE model. The photometric points are colour coded based on their dropout sample as defined in Fig. 1. The weak lines and extremely blue UV slopes imply low amounts of nebular emission, indicative of high f_{esc} within these galaxies.

extremely blue UV slopes preferentially identifies galaxies with the least impact from dust, which may bias our sample toward lower masses. Thus, the typically low masses found for our sample does not necessarily indicate that somewhat higher mass galaxies cannot also have significant escape fractions.

We explore the sizes of our extremely blue sample to investigate the geometrical and morphological characteristics of this candidate population of leakers. Sizes were derived from the *JWST*/NIRCam mosaics for each galaxy in the filter covering rest-frame 1500 Å using the method outlined in Chen et al. (2023). We utilize the inferred sizes to quantify the SFR surface densities ($\Sigma_{SFR} = SFR/2\pi r_e^2$), which are often thought to yield favourable conditions for f_{esc} at high Σ_{SFR} (e.g. Sharma et al. 2017). The measured sizes and SFRs derived from the SED modelling for our extremely blue sample are shown in Fig. 11. A majority (25/44) of the sample is unresolved implying compact sizes of ≤ 160 pc, while the remaining objects (19/44) have a median effective radius of 326 pc, and up to 800 pc for the most extended object. Among the resolved galaxies, we find a median Σ_{SFR} of $1.4\,M_\odot$ yr^{-1} kpc^{-2}. The remaining unresolved galaxies are all limited to above this value, in agreement with results at $z >$ 10, which have found values of 15–180 $M_\odot$ yr^{-1} kpc^{-2} (Robertson et al. 2023b). We compare our results to galaxies with confirmed LyC leakage at lower redshift including the Low-redshift Lyman Continuum Survey (LzLCS; Flury et al. 2022a, b) and Keck Lyman Continuum Spectroscopic Survey (Kim et al. 2023). In these cases, higher resolution from lensing is still required to better link the measured very blue UV slope and associated SFR surface density.

4.3 The influence of bursty SFHs on very blue UV slopes

It is commonly assumed that LyC leakage is the primary physical interpretation driving extremely blue ($\beta < -2.8$) UV slopes in star-forming galaxies. Here we consider whether short-term variations in the instantaneous SFR may provide an alternative explanation. Theoretical studies have indicated that 'bursty' SFHs are likely common in galaxies at early times (e.g. Faucher-Giguère 2018; Ma et al. 2020; Tacchella, Forbes & Caplar 2020; Furlanetto & Mirocha 2022; Mirocha & Furlanetto 2023; Dome et al. 2024). Observations with *JWST* are providing new evidence that this may be the case (Dressler et al. 2023; Endsley et al. 2023b; Looser et al. 2023; Strait et al. 2023; Tacchella et al. 2023). Shortly following the cessation of star formation after a burst, the overall ionizing photon production falls. As a result, the nebular continuum strength decreases, allowing the stellar continuum to dominate in the UV. This enables very
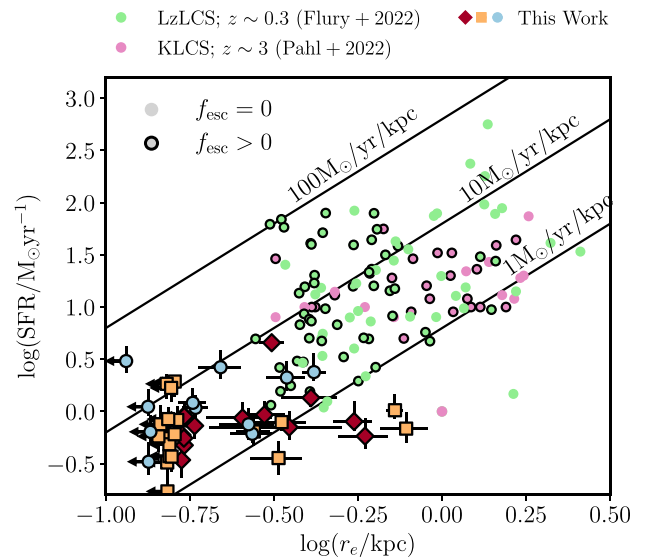

Figure 11. SFRs derived from the best-fitting BEAGLE models as a function of effective radius measured from the NIRCam mosaics. The radii presented here are measured for each object in the filter corresponding to rest-frame 1500 Å. We display and label lines of constant SFR surface density (Σ_{SFR}). Points in our sample are displayed using the same scheme as in previous figures. For comparison, we display objects from the LzLCS (Flury et al. 2022a) comprising a sample of $z \sim 0$ galaxies, in addition to a sample of galaxies at $z \sim 3$ from Pahl et al. (2021). Galaxies in the low-redshift comparison samples with confirmed $f_{esc} > 0$ are outlined in black. The sources in our sample typically have much smaller SFRs and are more compact compared to the low-redshift objects.

blue UV slopes to be observed. In what follows, we explore the possibility of this physical picture as an avenue to describe the observed SEDs of our extremely blue sample, and discuss the impact on our interpretation of these sources.

We first explore whether UV slopes can reach sufficiently blue values after a burst of star formation. We quantify the time evolution of UV slopes using mock SEDs constructed with BEAGLE. In Fig. 12, we display the expected UV slopes for simple stellar population (SSP) models, compared to models assuming a CSFH calculated at $f_{esc} = 0$ and 0.75. After a time lag of ~ 5 Myr following the cessation of star formation, the reduction of the nebular continuum becomes significant, resulting in bluer UV slopes compared to the
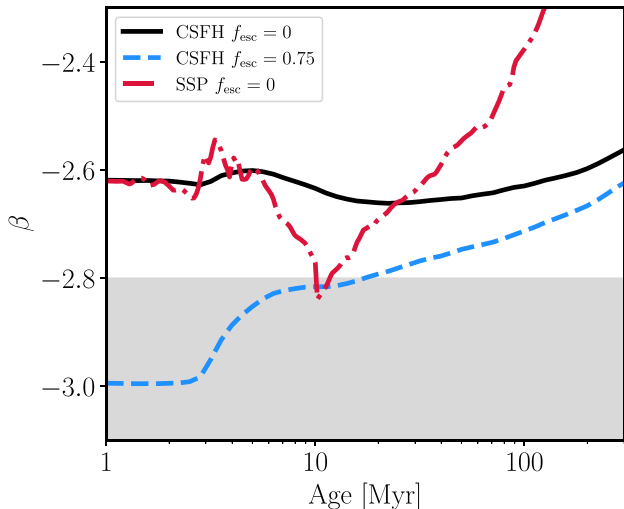
Figure 12. Evolution of the UV slopes as a function of galaxy age calculated from SED models constructed using BEAGLE. Each model is calculated assuming a $\log(U) = -2.5$, metallicity of 10 per cent $Z_\odot$, and no dust attenuation. We present UV slopes for a CSFH at $f_{esc} = 0$ (black line), $f_{esc} = 0.75$ (blue dashed line), and an SSP with $f_{esc} = 0$ (red dash–dotted line). We shade the region of the figure ($\beta < -2.8$) coincident with our extremely blue galaxy sample.

CSFH models. The UV slopes continue to decrease up to an age of 10 Myr, reaching a minimum β of -2.8. Following this minimum, the population becomes increasingly composed of less massive stars that have intrinsically redder UV spectra. Thus, for ages of $\simeq 5$–30 Myr, the burst models are able to produce UV slopes bluer than those possible with the CSFH models alone. Based on these results, we find that the UV slopes of an SSP can reach a very blue value similar to that of a density-bounded model with an $f_{esc} = 0.75$. However, this only occurs for a short period of time after the burst.

We apply this physical picture to our sample of very blue galaxies using models with a two-component star formation history (TcSFH) such as those described in Endsley et al. (2023b). Briefly, these models decouple the SFR over the most recent 20 Myr from previous star formation that may be present, while keeping the remaining model parameters the same as our model set-up described in Section 2.3. This allows for both upturns and lulls in recent star formation. Systematically, modelling the extremely blue sources with the TcSFH models does result in better fits to the observed data when compared to the CSFH models with $f_{esc} = 0$. The reduced χ^2 from the TcSFH model fits of the very blue sources range from 0.3 to 10.3, with a median of 2.0. This measure represents an improvement upon the model fits assuming $f_{esc} = 0$ and a CSFH; however, these models do not surpass the $f_{esc} > 0$ in their ability to reproduce the observed SEDs.

Fig. 13 compares the best-fitting SEDs derived assuming a CSFH with non-zero escape fraction to the TcSFH model. Among these examples, it is clear that the UV continua of galaxies with $\beta \simeq -2.8$ can be fit well by the TcSFH models; however, the objects with bluer UV slopes are still challenging to reproduce without invoking LyC photon escape. It is clear from the SEDs shown in Fig. 13 that the TcSFH models indicate significantly stronger rest-optical continuum levels than the density-bounded models. This in turn leads to the TcSFH stellar masses being systematically larger than those derived from the density-bounded models. Quantitatively, we find an increase in stellar mass of 0.3 dex on average, though the most extreme

cases lead to an increase of 0.8 dex. Ultimately, deep spectroscopy capable of detecting the continuum level in these sources should help distinguish between these scenarios for the very blue UV slopes.

5 SUMMARY

In this paper, we have leveraged deep *JWST*/NIRCam imaging from the JADES program to explore the UV slopes for a statistical sample of galaxies up to $z \sim 14$. This sample covers a wide range of redshifts ($z \sim 5$–14) and UV luminosities ($M_{UV} = -22$ to -16), allowing us to explore trends between UV slopes and galaxy properties at high redshift. Furthermore, we leverage both the wide areas and deep exposure times of JADES to identify rare $\beta \simeq -3$ galaxies, providing insight into some of the most extreme objects in the reionization era. We summarize our main results below.

(i) We measured UV slopes for 1276 galaxies identified within deep *JWST*/NIRCam imaging from JADES, comprising four dropout samples spanning a range of redshifts from $z \simeq 5$ to $z \simeq 14$. The UV slopes of these high-redshift galaxies are typically blue, with median values of $\beta = -2.26^{+0.03}_{-0.03}$, $\beta = -2.32^{+0.03}_{-0.02}$, $\beta = -2.35^{+0.04}_{-0.04}$, and $\beta = -2.48^{+0.12}_{-0.14}$ at a redshift of $z \sim 5.9$, $z \sim 7.3$, $z \sim 9.4$, and $z \sim 12.02$, respectively. We divide each of the three lower redshift dropout samples into bins of M_{UV} and explore how the typical UV slopes vary with UV luminosity. This test reveals that throughout the redshift range sampled here, galaxies with lower UV luminosities typically display bluer UV slopes. Using a set of simple analytic simulations, we find that this trend is not explained by biases resulting from reduced efficiency of selecting redder galaxies.

(ii) At fixed UV luminosity we find that the average UV slopes become bluer in higher redshift samples. We find that the rate of this evolution is slowest (fastest) at low (high) UV luminosities. Galaxies at $z > 9$ and $M_{UV} = -18$ display only minor UV slope differences compared to the $z \simeq 5$–9 population, while at an $M_{UV} = -20$ we find significant evolution toward bluer UV slopes corresponding to $\Delta\beta = -0.15$. The asymptotic behaviour of typical UV slopes at lower luminosities suggests that the population is becoming increasingly saturated by galaxies approaching the intrinsic UV slope limit. At yet higher redshift, we find increased evolution toward bluer UV slopes. We find that galaxies at $z \sim 12$ display a typical UV slope of $\beta = -2.48^{+0.14}_{-0.12}$, compared to the $z \simeq 9$ population which are just $\beta = -2.33^{+0.09}_{-0.08}$. This implies that galaxies at the highest redshifts are subject to very little impact from dust.

(iii) The total fraction of galaxies with moderately red UV slopes ($\beta > -2$) decreases with redshift, and sharply falls off at $z \gtrsim 11$. Such objects comprise 22.8, 17.5, and 19.4 per cent of the population at $z \simeq 5.86$, $z \simeq 7.28$, and $z \simeq 9.41$, respectively. In contrast, the contribution of such sources to the highest redshift sample at $z \sim 12$ is only 5 per cent, as only one object falls into this category. Notably, a similar decrease at $z \gtrsim 12$ is found among galaxies selected primarily on their photometric redshifts, suggesting that selection effects are not the principal cause for this evolution.

(iv) We identify a sample of 44 galaxies with extremely blue UV slopes ($\beta < -2.8$) that we classify as robust based on a set of criteria developed to maximize the likelihood that they are genuine. This sample is composed of galaxies spanning redshifts of $z_{phot} = 5.42$–10.96 and UV luminosities corresponding to $M_{UV} = -19.7$ to -17.2, and comprise 3.4 per cent of the total sample. We find that the SEDs of this extremely blue sample are well described by models of density-bounded H II regions with an average f_{esc} of 0.51.

(v) We search for evidence that the extremely blue samples display weak emission lines, which is expected if they exhibit high fractions of ionizing photon leakage. We use colour excesses to infer the
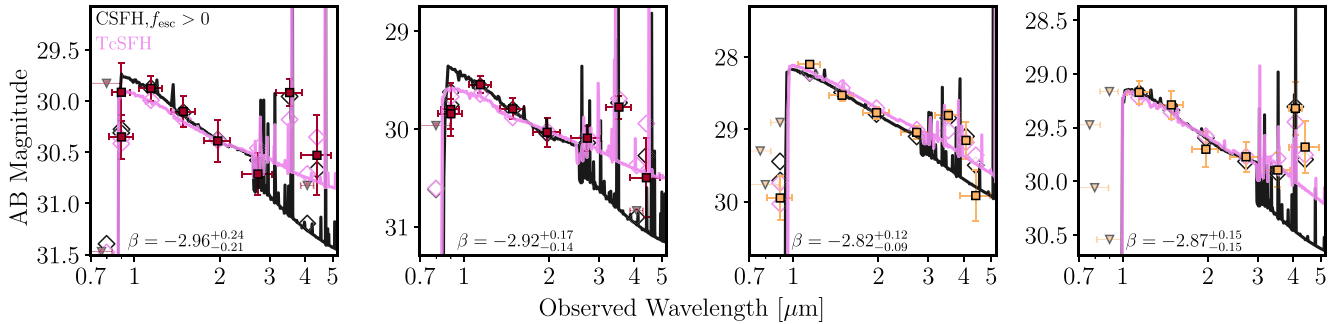
Figure 13. Comparison of best-fitting SEDs when modelled as a density-bounded H II region with a CSFH (black) and a two-component SFH characterized by a recent cessation of star formation (pink). The photometric fluxes predicted from each of the models are shown as the empty diamonds. The observed fluxes and uncertainties are displayed as the red and orange points for objects that are *F775W* and *F090W* dropouts, respectively.

emission line strengths of our sample, and find that the median *F356W* − *F444W* colour of our extremely blue sample is 0.19 mag, which is systematically below the median of 0.39 mag found for the full sample. This implies that the extremely blue objects have weaker lines on average than the typical galaxies at this redshift, which is in line with the high values of f_{esc} inferred for the sample. Model fits to this sample imply that they are characterized by very high sSFRs (median 79 Gyr^{-1}), which are systematically elevated relative to the full sample of galaxies selected here (median 44 Gyr^{-1}). Furthermore, we infer stellar masses of the extremely blue sample in the range $\log(M/M_\odot) = 7.0$–8.5 (median $\log(M/M_\odot) = 7.5 \pm 0.2$), which is consistent with simulation predictions for leakers.

(vi) Finally, we explore the SEDs of the extremely blue sample in context of models where recent star formation is decoupled from past star formation. We find that the cessation of star formation is able to produce UV slopes bluer than that of CSFH models with $f_{esc} = 0$ on short time-scales, and provide a better fit to the data on average. However, the χ^2 of the complex SFH models are not as good as those of the high f_{esc} models. The resulting model fits imply stellar masses in excess of the high f_{esc} models by 0.3 dex on average, with a maximum offset of 0.8. However, in many cases, the complex SFHs require significant past star formation that have a stronger rest-optical continuum level relative to the density-bounded models and observed photometry.

Using *JWST*, we have constructed statistical samples of high-redshift galaxies, unveiling the properties of typical galaxies at $z \gtrsim 9$, in addition to identifying rare and extreme galaxies. Future campaigns providing spectroscopy of these sources will be a crucial step forward unveiling the nature of these galaxies with extremely blue UV slopes ($\beta < -2.8$). Such data will confirm the UV slopes of the extremely blue systems, and will constrain the emission line EWs in a way that does not rely on model assumptions. Further analysis of their spectra can shed light on the physical processes driving their extremely blue colours, and will cement their place among galaxies responsible for cosmic reionization.

DATA AVAILABILITY

A portion of the observations utilized in this work can be accessed online at DOI: 10.17909/8tdj-8n28. The remaining data underlying this article will be shared on reasonable request to the corresponding author.

REFERENCES

Arrabal Haro P. et al., 2023, ApJ, 951, L22
Asplund M., Grevesse N., Sauval A. J., Scott P., 2009, ARA&A, 47, 481
Bagley M. B. et al., 2023, ApJ, 946, L12
Bertin E., Arnouts S., 1996, A&AS, 117, 393
Bhatawdekar R., Conselice C. J., 2021, ApJ, 909, 144
Bouwens R. J. et al., 2010, ApJ, 708, L69
Bouwens R. J. et al., 2012, ApJ, 754, 83
Bouwens R. J. et al., 2014, ApJ, 793, 115
Bouwens R. J. et al., 2015, ApJ, 803, 34
Bouwens R. J. et al., 2016, ApJ, 833, 72
Bouwens R. J., Illingworth G. D., Ellis R. S., Oesch P. A., Stefanon M., 2022, ApJ, 940, 55
Brammer G. B., van Dokkum P. G., Coppi P., 2008, ApJ, 686, 1503
Bruzual G., Charlot S., 2003, MNRAS, 344, 1000
Calabrò A. et al., 2021, A&A, 646, A39

Calzetti D., Kinney A. L., Storchi-Bergmann T., 1994, ApJ, 429, 582

Chabrier G., 2003, PASP, 115, 763

Chen Z., Stark D. P., Endsley R., Topping M., Whitler L., Charlot S., 2023, MNRAS, 518, 5607

Chevallard J., Charlot S., 2016, MNRAS, 462, 1415

Chisholm J. et al., 2022, MNRAS, 517, 5104

Cullen F., McLure R. J., Khochfar S., Dunlop J. S., Dalla Vecchia C., 2017, MNRAS, 470, 3006

Cullen F. et al., 2023, MNRAS, 520, 14

Curtis-Lake E. et al., 2023, Nat. Astron., 7, 622

Dome T., Tacchella S., Fialkov A., Ceverino D., Dekel A., Ginzburg O., Lapiner S., Looser T. J., 2024, MNRAS, 527, 2139

Dressler A. et al., 2023, preprint (arXiv:2306.02469)

Dunlop J. S., McLure R. J., Robertson B. E., Ellis R. S., Stark D. P., Cirasuolo M., de Ravel L., 2012, MNRAS, 420, 901

Eisenstein D. J. et al., 2023, preprint (arXiv:2306.02465)

Endsley R., Stark D. P., Whitler L., Topping M. W., Chen Z., Plat A., Chisholm J., Charlot S., 2023a, MNRAS, 524, 2312

Endsley R. et al., 2023b, preprint (arXiv:2306.05295)

Faucher-Giguère C.-A., 2018, MNRAS, 473, 3717

Ferrara A., Pallottini A., Dayal P., 2023, MNRAS, 522, 3986

Finkelstein S. L. et al., 2012, ApJ, 756, 164

Flury S. R. et al., 2022a, ApJS, 260, 1

Flury S. R. et al., 2022b, ApJ, 930, 126

Furlanetto S. R., Mirocha J., 2022, MNRAS, 511, 3895

Furtak L. J., Shuntov M., Atek H., Zitrin A., Richard J., Lehnert M. D., Chevallard J., 2023, MNRAS, 519, 3064

Gardner J. P. et al., 2023, PASP, 135, 068001

Giavalisco M. et al., 2004, ApJ, 600, L93

Gutkin J., Charlot S., Bruzual G., 2016, MNRAS, 462, 1757

Hainline K. N. et al., 2024, ApJ, 64, 71

Harikane Y., Nakajima K., Ouchi M., Umeda H., Isobe Y., Ono Y., Xu Y., Zhang Y., 2024, ApJ, 960, 56

Heckman T. M. et al., 2011, ApJ, 730, 5

Illingworth G. D. et al., 2013, ApJS, 209, 6

Jiang L., Cohen S. H., Windhorst R. A., Egami E., Finlator K., Schaerer D., Sun F., 2020, ApJ, 889, 90

Kim K. J. et al., 2023, ApJ, 955, L17

Kron R. G., 1980, ApJS, 43, 305

Labbé I. et al., 2010, ApJ, 716, L103

Looser T. J. et al., 2023, preprint (arXiv:2306.02470)

Ma X., Quataert E., Wetzel A., Hopkins P. F., Faucher-Giguère C.-A., Kereš D., 2020, MNRAS, 498, 2001

McLure R. J. et al., 2011, MNRAS, 418, 2074

Mason C. A., Trenti M., Treu T., 2023, MNRAS, 521, 497

Mirocha J., Furlanetto S. R., 2023, MNRAS, 519, 843

Naidu R. P., Tacchella S., Mason C. A., Bose S., Oesch P. A., Conroy C., 2020, ApJ, 892, 109

Nanayakkara T. et al., 2023, ApJ, 947, L26

Oke J. B., Gunn J. E., 1983, ApJ, 266, 713

Ono Y., Ouchi M., Shimasaku K., Dunlop J., Farrah D., McLure R., Okamura S., 2010, ApJ, 724, 1524

Pahl A. J., Shapley A., Steidel C. C., Chen Y., Reddy N. A., 2021, MNRAS, 505, 2447

Pahl A. J., Shapley A., Steidel C. C., Reddy N. A., Chen Y., Rudie G. C., Strom A. L., 2023, MNRAS, 521, 3247

Pei Y. C., 1992, ApJ, 395, 130

Plat A., Charlot S., Bruzual G., Feltre A., Vidal-García A., Morisset C., Chevallard J., Todt H., 2019, MNRAS, 490, 978

Raiter A., Schaerer D., Fosbury R. A. E., 2010, A&A, 523, A64

Reddy N. A. et al., 2018, ApJ, 869, 92

Rieke M. J., Kelly D., Horner S., 2005, in Heaney J. B., Burriesci L. G., eds, Proc. SPIE Conf. Ser. Vol. 5904, Cryogenic Optical Systems and Instruments XI. SPIE, Bellingham, p. 1

Rieke M. J. et al., 2023a, ApJS, 269, 16

Rieke M. J. et al., 2023b, PASP, 135, 028001

Rigby J. et al., 2023, PASP, 135, 048001

Robertson B. E., Ellis R. S., Dunlop J. S., McLure R. J., Stark D. P., 2010, Nature, 468, 49

Robertson B. et al., 2023a, preprint (arXiv:2312.10033)

Robertson B. E. et al., 2023b, Nat. Astron., 7, 611

Rogers A. B., McLure R. J., Dunlop J. S., 2013, MNRAS, 429, 2456

Rosdahl J. et al., 2022, MNRAS, 515, 2386

Saldana-Lopez A. et al., 2023, MNRAS, 522, 6295

Sharma M., Theuns T., Frenk C., Bower R. G., Crain R. A., Schaller M., Schaye J., 2017, MNRAS, 468, 2176

Strait V. et al., 2023, ApJ, 949, L23

Tacchella S., Forbes J. C., Caplar N., 2020, MNRAS, 497, 698

Tacchella S. et al., 2022, ApJ, 927, 170

Tacchella S. et al., 2023, ApJ, 952, 74

Topping M. W. et al., 2022, MNRAS, 516, 975

Treu T. et al., 2023, ApJ, 942, L28

Whitaker K. E. et al., 2019, ApJS, 244, 16

Wilkins S. M., Bunker A. J., Stanway E., Lorenzoni S., Caruana J., 2011, MNRAS, 417, 717

Wilkins S. M., Bouwens R. J., Oesch P. A., Labbé I., Sargent M., Caruana J., Wardlow J., Clay S., 2016, MNRAS, 455, 659

Williams C. C. et al., 2023, ApJS, 268, 64

Willott C. J. et al., 2023, preprint (arXiv:2311.12234)

Yamanaka S. et al., 2020, MNRAS, 498, 3095

Yung L. Y. A., Somerville R. S., Finkelstein S. L., Wilkins S. M., Gardner J. P., 2024, MNRAS, 527, 5929

Zackrisson E., Inoue A. K., Jensen H., 2013, ApJ, 777, 39

Zackrisson E. et al., 2017, ApJ, 836, 78

This paper has been typeset from a TEX/LATEX file prepared by the author.